Real-time Bayesian damage identification enabled by sparse PCE-Kriging meta-modelling for continuous SHM of large-scale civil engineering structures

Enrique García-Macías[a,b,*], Filippo Ubertini[a]

[a] *Department of Civil and Environmental Engineering, University of Perugia. Via G. Duranti, 93 - 06125 Perugia, Italy.*
[b] *Department of Structural Mechanics and Hydraulic Engineering, University of Granada, Av. Fuentenueva sn, 18002 Granada, Spain.*

Abstract

This work presents a surrogate model-based Bayesian model updating (BMU) approach for automated damage identification of large-scale structures, which outperforms methods currently available in the literature by effectively solving the real-time damage identification challenge. The computational difficulties involved in Bayesian inference using intensive numerical models are circumvented by implementing a high-fidelity surrogate model and an adaptive Markov Chain Monte Carlo (MCMC) algorithm. The developed surrogate model combines adaptive sparse polynomial chaos expansion (PCE) and Kriging meta-modelling. The optimal order of the polynomials in the PCE is automatically identified by a model selection technique for sparse linear models, the least-angle regression (LAR) algorithm. Then, the optimal PCE is inserted into a Kriging predictor as the trend term, while the stochastic term is fitted through a global optimization algorithm. Afterwards, the surrogate model bypassing the original numerical model is used for BMU exploiting monitoring data extracted from continuous ambient vibration measurements. The computational demands of the MCMC algorithm are kept minimal by implementing an adaptive Metropolis sampling with delayed rejection (DRAM). The effectiveness of the proposed methodology is demonstrated through three case studies: an analytical benchmark; a planar truss structure; and a real case study of an instrumented historical tower, the Sciri Tower in Italy. The presented results demonstrate that the proposed BMU approach is compatible with real-time Structural Health Monitoring (SHM), providing promising evidence for the development of digital twins with superior probabilistic damage identification capabilities.

Keywords: Damage localization, Bayesian inference, Operational Modal Analysis, Structural health monitoring, Surrogate models.

1. Introduction

The concern for the management of ageing infrastructure has substantially increased over recent years after tragic collapses such as Genoa bridge (Italy, 2018) [1] or the Nanfang'ao Bridge (Taiwan, 2019). Nonetheless, the economic downturn derived from the COVID-19 pandemic has exacerbated the existing underinvestment in public infrastructure worldwide, which remains far below the levels prior to the 2007-2008 financial crisis [2]. Evidence of this is the last Infrastructure Report Card by the American Society of Civil Engineers [3] which, despite reporting improvements with respect to previous reports rating the US infrastructure as "D+" or in an overall poor condition, assigned a grade of "C-" or in fair to good condition with general signs of deterioration. Among the evaluated categories, the report indicated that 7.5% of the American bridges are in poor conditions and estimated the nation's backlog of bridge repair at $123 billion. The daunting challenge of addressing ageing infrastructure and its profound impact on the social and economic fabric has been reflected in a number of infrastructure maintenance plans (see e.g. [4]), and increases in funding efforts devoted to R&D in the realm of SHM. It is worth stressing the new guidelines for the classification, risk assessment, safety evaluation, and monitoring of bridges approved by the Italian Ministry of Infrastructures and Transport in May 2020 [5], which highlights the important role of SHM.

In the broadest sense, SHM exploits long-term monitoring data to track anomalies in the structural performance caused by damage and, desirably, to predict the structural life expectancy [6]. Among the available technologies, ambient vibration-based SHM has become particularly widespread owing to its non-destructive nature and minimum intrusiveness, as it is enabled by relatively low-cost acceleration sensors, requires no artificial excitation, and causes no disruption to the normal fruition of the assets [7]. Typically, these techniques encompass Operational

*Corresponding author. Department of Civil and Environmental Engineering, University of Perugia. Via G. Duranti, 93 - 06125 Perugia, Italy. phone: +39 075 585 3908; fax: +39 075 585 3897

Email addresses: enrique.garciamacias@unipg.it (Enrique García-Macías), filippo.ubertini@unipg.it (Filippo Ubertini)

Modal Analysis (OMA) methods fitting linear systems from response acceleration measurements of structures subjected to non-measured stationary ambient excitations (e.g. wind, traffic, micro-tremors) [8–10]. This allows one to extract the modal features of the structure under study (i.e. natural frequencies, mode shapes, and damping ratios), which are directly related to its mass/stiffness and energy dissipation features and, therefore, are sensitive to structural damage. Damage identification is commonly organized in a hierarchical structure of increasing complexity, including (i) Detection; (ii) Localization; (iii) Classification; (iv) Extension; and (v) Prognosis. Generally, damage identification approaches are classified in three categories [11]: unsupervised learning (UL), supervised learning (SL), and semi-supervised learning (SSL). Supervised techniques are those trained with data from both the undamaged and damaged structure, while only information on the undamaged structure is used to train UL models. Semi-supervised learning represents an intermediate solution when a certain amount of training data tagged as "damaged" is available, although not sufficient for full SL. In this light, UL techniques have been more extensively used due to the intrinsic difficulties stemming from obtaining data from damage states, and various successful applications can be found in the literature (see e.g. [12, 13]). Unfortunately, a major drawback is that UL usually limits to damage detection (i). This diagnostic level may result insufficient when planning the maintenance of highly critical structures (e.g. hospitals, dams, or power industry facilities). In those cases, gaining insight into the damage location and extension is paramount for maintenance prioritization under tight budgetary constraints, as well as the mobilization of emergency services, evacuation, and interruption of structures affected by natural disasters. Nevertheless, collecting tagged data (damage/undamaged) in SL is always a challenging task, either through modelling or experiments. The use of numerical models is often the only viable solution, since making physical copies of large-scale structures to induce controlled damage is simply infeasible. In this regard, Structural Identification (St-Id) or model updating aims to bridge the gap between theoretical models and real systems by tuning the model parameters in such a way that the mismatch amidst experimental and theoretical observations is minimized. However, potential end-users remain sceptical about the usefulness of St-Id for the maintenance of civil infrastructure, being chiefly due to the extensive use of simplistic and prescriptive models for St-Id in the literature [14]. In particular, one of the major obstacles for the extensive implementation of St-Id in engineering practice stems from the difficulties involved in the use of computationally intensive numerical models into automated long-term SHM systems.

Broadly speaking, St-Id techniques aim to identify unknown properties of the structure under study which appear as parameters in a theoretical model by exploiting data acquired from field tests. These may include material parameters, geometric properties, boundary conditions and/or connectivity, for which conjectures and simplifying assumptions necessarily have to be made due to the inevitable existence of aleatory and epistemic uncertainties. These techniques can be also conceived as non-destructive damage assessment methods, when attributing defects to damage-induced differences between the identified model parameters and in-control or design values [15]. One of the most challenging aspects involved in model updating regards its proneness to ill-posedness and ill-conditioning [16]. Such effects imply a loss of convexity, and therefore the existence, uniqueness and stability of a solution of the inverse problem cannot be guaranteed. Overall, methods for model updating can be categorized into deterministic and probabilistic or uncertainty quantification (UQ) approaches [17]. Deterministic methods are relatively mature and a large number of successful applications can be found in the literature (see e.g. [18, 19]). These methods determine a unique solution by solving an optimization problem, which typically minimizes a non-linear objective function accounting for the discrepancies between theoretical models and experimental data. To address ill-conditioning and ill-posedness, regularisation and parametrisation are often adopted [16]. Common regularisation approaches are variations of the classical Tikhonov regularisation, which introduces an additive constraint to the objective function in the form of a model norm scaled by a Lagrange multiplier (see e.g. [20]). A suitable parametrization of the model is also a key aspect to minimize ill-conditioning. In general terms, it is critical to choose those parameters for which the model output is particularly sensitive. Sensitivity analysis constitutes the simplest and most intuitive approach [21], although more sophisticated parametrization methods can be found in the literature such as variance-based global sensitivity analysis [22], sensitivity-based parameter clustering [23], and more.

Despite deterministic St-Id methods are in general intuitive and require moderate computational efforts, a major limitation relates to their inability to handle uncertainties. This hinders their implementation into condition-based maintenance schemes, since no evidence on the reliability of the model nor the robustness of decisions made from its predictions can be obtained. Alternatively, UQ models not only allow assessing the effects of uncertainty on the updated model parameters, but also provide means to evaluate the uncertainties on derived quantities such as response predictions [24]. In this light, BMU methods are becoming especially popular owing to their ability to address uncertainties, robustness to the presence of noise in the measurements, and efficiency to handle ill-conditioning limitations. The latter is achieved by specifying prior probability distribution functions (PDFs) over the uncertain parameters, which imposes a regularization to the inverse problem. Such excellent features have fostered their implementation to multiple structural systems (refer to [25, 26] for an extensive state-of-the-art review).

The evaluation of the posterior PDFs requires solving a possibly high-dimensional integral which, except for some trivial cases, needs to be approximated numerically. Markov chain methods are usually implemented to extract series of samples to estimate the posterior PDFs, allowing to sample from a large class of high-dimensional distributions. Popular procedures for Markov Chain Monte Carlo (MCMC) sampling are the Metropolis-Hastings [27] and Gibbs algorithms [28], although a variety of more efficient sampling algorithms have been proposed in recent years [29], including Transitional MCMC (TMCMC) [30], BMU with Structural Reliability [31], Bayesian broad learning (BBL) [32], hybrid particle swarm MCMC [33], and Sparse Bayesian Learning [34], among others. Notwithstanding the rapid progress of BMU techniques, their elevated computational cost (commonly orders-of-magnitude higher than deterministic methods) remains a critical limitation, which explains that most of the existing researches focus on laboratory case studies. Amongst the works dealing with BMU of large-scale civil structures, it is worth stressing the work by Sun *et al.* [35] who adopted a hierarchical Bayesian framework with MCMC to calibrate a finite element model (FEM) of a 21-storey building located in Cambridge (USA). To do so, those authors defined a likelihood function exploiting differences between experimental and numerical impulse response functions obtained through ambient noise deconvolution interferometry. Behmanesh and Moaveni [36] proposed a hierarchical Bayesian BMU for the identification of the Downling Hall footbridge located in Somerville (USA) under changing environmental conditions. In particular, those authors defined a likelihood function accounting for resonant frequencies and mode shapes estimated by a continuous OMA system installed in the bridge for over 27 months, and demonstrated the ability of the proposed technique to identify several damage scenarios simulated through added masses. Bartoli and co-authors [37] performed the BMU of a FEM of a historical tower, the Becci tower in Italy, by exploiting experimentally identified resonant frequencies. The calibrated model was then used to obtain stochastic fragility curves and assess the seismic vulnerability of the tower. Zhou *et al.* [38] applied a BMU method based on TMCMC for damage identification of a simply supported steel truss bridge. Interestingly, before its demolition in 2012, four controlled damage scenarios were induced in the bridge and several ambient vibration tests (AVTs) were conducted to identify its modal signatures. The reported results and discussion demonstrated the ability of the proposed BMU method to identify the four induced damage scenarios when a suitable parametrization of the underlying numerical model is defined.

In light of the previous discussion, the major constraint of BMU methods stems from their considerable computational demands due to the sheer number of iterations required for convergence. As a result, the computational cost of BMU of complex large-scale civil structures becomes unaffordable and definitely incompatible with real-time SHM systems. To tackle such a challenge, recent advances in the development of high-fidelity surrogate models have brought a new horizon for real-time St-Id. Indeed, a broad variety of surrogate modelling methods have been successfully applied in the context of St-Id, including Response surface models (RSMs) [39], PCE [40], Support Vector Regression [41], and Kriging [42], as well as techniques from Machine Learning (ML) such as Gaussian process approximation [43], or Artificial Neural Networks [44]. For instance, Pepi *et al.* [45] developed a PCE surrogate model of the modal properties of a cable-stayed footbridge in Terni (Italy), and implemented an MCMC BMU algorithm to identify the model parameters of the bridge. Schneider *et al.* [46] proposed a BMU procedure using rational PCE meta-models of the response of dynamic systems in the frequency domain, and demonstrated its effectiveness for the St-Id of a cross-laminated timber plate. Alternatively to the use of surrogate models to bypass computationally intense numerical models, Han and co-authors [47] proposed the use of PCE to approximate the likelihood function used in the BMU of a laboratory eight-floor steel frame. Nonetheless, most research works limit to St-Id applications using experimental measurements from isolated tests, while investigations coping with continuous SHM data are much more scarce. In this regard, a noteworthy contribution was made by Cabboi *et al.* [48], who reported the deterministic RSM-based damage identification of a stone-masonry tower exploiting continuous time series of resonant frequencies extracted by automated OMA. In this line, recent contributions by the authors [49, 50] presented the development of an online surrogate model-based deterministic St-Id approach for damage identification of a historical tower, the Sciri Tower in Perugia (Italy). Through an objective function exploiting modal signatures obtained by automated OMA, the reported St-Id results proved compatible with real-time SHM. Finally, damage assessment was conducted through pattern recognition and novelty analysis adopting the model updating parameters as damage-sensitive features. Ierimonti and co-authors [51] proposed a conjugate BMU methodology for online damage identification of an instrumented monumental building, the Consoli Palace in Gubbio (Italy). Through the construction of Kriging meta-models bypassing a 3D FEM of the palace, BMU was applied to daily data-sets of resonant frequencies and mode shapes identified by automated OMA during about 5 months. The reported results demonstrated the ability of the proposed approach to localize and quantify synthetic damage scenarios in probabilistic terms.

In spite of the encouraging results discussed above, the implementation of continuous MCMC BMU of for SHM applications remains virtually unexplored. Specifically, no evidences have been reported in the literature on successful applications of continuous Bayesian damage identification of large scale-civil engineering structures under varying environmental conditions. This is primarily due to the formidable computational challenge involved in the sampling of the posterior PDF. To address such a challenge, this work proposes a new methodology combining high-fidelity surrogate models and MCMC compatible with real-time SHM. The proposed surrogate model combines adaptive sparse PCE and Kriging meta-modelling. The choice of this surrogate modelling strategy is motivated by its generality and versatility. While PCE handles the global behaviour of the model, Kriging is particularly well-suited to model local variations, attaining both local and global modelling capabilities when combined [52]. The LAR algorithm proposed by Efron and co-authors [53] is adopted to automatically define the optimal order of the PCE and minimize the number of terms in the expansion, thus keeping minimal the computational burden involved in the training and evaluation of the meta-model. The optimized PCE is then introduced into a Kriging predictor as the trend term, while the stochastic term is fitted through a genetic algorithm (GA) global optimization approach. On the other hand, the main difficulties involved in BMU comprise: (i) finding the regions of significant probability of the posterior PDF in high-dimensional parameter spaces, and (ii) sampling from multimodal PDFs. The proposed method circumvents these difficulties by implementing the DRAM MCMC approach, which combines adaptive Metropolis (AM) sampling and delayed rejection (DR). While AM provides global adaptation capabilities by tuning the proposal distribution from the past history of the chain, the RD algorithm offers local adaptation of the proposal distribution based on rejected samples within each step. The effectiveness of the proposed methodology is demonstrated through three case studies: (i) an analytical benchmark; (ii) a numerical planar truss structure; and (iii) a real case study of a historical masonry tower, the Sciri Tower. The Sciri Tower is a civic tower located in the city of Perugia (Italy) that was continuously instrumented during three weeks with an environmental/dynamic SHM system. The modal features of the tower have been extracted by automated OMA and used in the inverse calibration of a computationally intensive 3D FEM of the structure. The presented results prove that the proposed BMU approach for damage identification is compatible with real-time SHM under varying environmental conditions, which constitutes the main innovation of this work. The damage identification capabilities of the proposed approach are finally validated through several synthetic damage scenarios.

The remainder of this paper is organized as follows. Section 2 outlines the proposed surrogate model-based BMU for automated damage identification. Sections 3 and 4 overview the theoretical fundamentals of the developed sparse PCE-Kriging meta-model and BMU, respectively. Section 5 presents the numerical results and discussion and, finally, Section 6 concludes the paper.

2. General framework

The overarching purpose of the proposed approach is the continuous Bayesian St-Id of structures by exploiting continuous data-flows from permanent dynamic SHM systems. Typically, the monitoring system consists of a sensor network deployed on the structure of interest and of a data acquisition system (DAQ) that permanently collects the monitoring data. Subsequently, computer files containing monitoring records of certain time duration are sent to a server or to the cloud where the data are stored and processed. At this point, the outcomes of the processed signals are inserted into the newly proposed BMU approach. The general work-flow is sketched in Fig. 1 and comprises the following three consecutive steps:

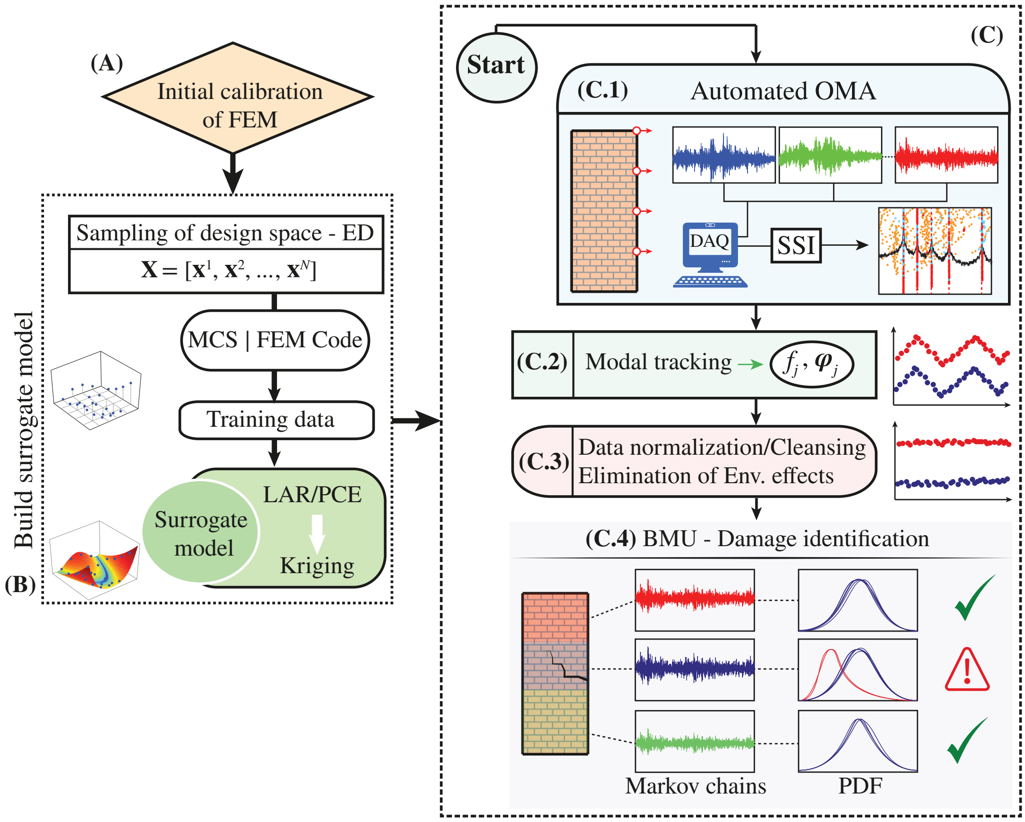

Figure 1: Flowchart of the proposed surrogate model-based continuous Bayesian St-Id approach.

(A): **Initial calibration of the FEM**: The initial FEM is constructed based on available structural drawings, on-site inspections, and geometrical/material surveys. Additionally, a series of assumptions typically need to be made, including boundary conditions, material homogeneity or structural connectivity. Therefore, the initial FEM may involve considerable sources of uncertainty that should be minimised before constructing the subsequent surrogate model. To contribute to this process, certain parameters of the FEM are calibrated using the modal properties determined by an initial AVT.

(B): **Construction of the surrogate model**: Based upon the previously tuned FEM, a surrogate model is constructed as a black-box function mapping between certain damage-sensitive model parameters contained in vector $\mathbf{x}$ and the modal signatures of the structure.

(C): **Automated surrogate model-based Bayesian damage identification**: This last step comprises the automated OMA of the structure, modal tracking, elimination of environmental effects, and surrogate model-based BMU. The first three sub-steps are routine practice in vibration-based SHM, so interested readers are referred to reference [54] for further theoretical details, while just a few highlights are reported below.

(C.1) Automated OMA: The modal features of the structure are identified through automated OMA of periodically recorded ambient vibrations.

(C.2) Modal tracking: This step is aimed at obtaining the time series of modal features of the structure by tracking a reference set of natural modes (typically obtained from an initial AVT) over the whole dataset of identified modal properties. The outcome of this stage at every step j comprises a set of resonant frequencies f_j and mode shapes φ_j.

(C.3) Data normalization and cleansing: The time series of modal signatures obtained in the previous step are usually highly affected by environmental and operational conditions (EOC). Such effects conceal the appearance of damage and need to be filtered out to attain effective damage identification. This is accomplished by training a pattern recognition model from an initial baseline dataset where the structure is assumed to remain in healthy conditions. Finally, the appearance of abnormal features due to identification and random errors can be eliminated through data cleansing techniques.

(C.4) Surrogate model-based BMU: The design variables at step j, $\mathbf{x}_j$, are fitted by the proposed BMU approach. Upon setting a statistical threshold associated with a certain confidence level, it is possible to trigger an alarm system when anomalies in the PDFs of the model parameters are detected. Since every design variable relates to the intrinsic stiffness of a specific element/region of the structure, anomalies in their PDFs directly indicate the location and severity of the damage.

3. Surrogate modelling

Let us consider a computational model $\mathcal{M}$ mapping between a vector of input variables $\mathbf{x} = [x_1, \dots, x_M]^{\mathrm{T}} \in \mathbb{R}^M$ (e.g. material and/or geometrical properties) and a certain quantity of interest or model response $y \in \mathbb{R}$ (e.g. modal property, local displacement), i.e. $y = \mathcal{M}(\mathbf{x})$. Within the context of this work, $\mathcal{M}$ is given by a computationally intensive FEM of the instrumented structure, and the output response y relates to a monitored or derived quantity. Note that in the case of a vector-valued model response, $\mathbf{y} = [y_1, \dots, y_Q]^{\mathrm{T}} \in \mathbb{R}^Q$, the following derivations hold component-wise.

3.1. Adaptive sparse polynomial chaos expansion

Assuming the components of $\mathbf{x}$ as independent random variables, the PCE representation of the output response is defined as an expansion of y onto an orthogonal multivariate polynomial basis as [55, 56]:

$$y = \mathcal{M}(\mathbf{x}) = \sum_{\boldsymbol{\alpha} \in \mathbb{N}^M} a_{\boldsymbol{\alpha}} \psi_{\boldsymbol{\alpha}}(\mathbf{x}), \tag{1}$$

where $a_{\boldsymbol{\alpha}}$ are unknown deterministic coefficients, and $\psi_{\boldsymbol{\alpha}}$ are multivariate polynomials. Given the statistical independence of the input random variables, the input joint PDF may be cast as:

$$f_{\mathbf{X}}(\mathbf{x}) = \prod_{i=1}^{M} f_{X_i}(x_i), \tag{2}$$

where $f_{X_i}(x_i)$ denotes the marginal PDF of x_i. A family of univariate polynomials $\left\{\psi_j^{(i)},\ j \in \mathbb{N}\right\}$ orthogonal with respect to f_{X_i} is adopted, that is:

$$\mathbb{E}\left[\psi_j^{(i)}(x_i)\,\psi_k^{(i)}(x_i)\right] = \int \psi_j^{(i)}(u)\,\psi_k^{(i)}(u) f_{X_i}(u)\,\mathrm{d}u = \delta_{jk}, \tag{3}$$

with δ_{jk} being the Kronecker delta operator. A variety of families of orthogonal polynomials have been proposed in the literature (see e.g. [57]), being the Legendre and Hermite polynomials the most commonly used ones for uniformly and normally distributed input variables x_i, respectively. Based upon the resulting M families of univariate polynomials, the basis of multivariate polynomials $\left\{\psi_{\boldsymbol{\alpha}},\ \boldsymbol{\alpha} \in \mathbb{N}^M\right\}$ is defined as:

$$\psi_{\boldsymbol{\alpha}}(\mathbf{x}) = \prod_{i=1}^{M} \psi_{\alpha_i}^{(i)}(x_i), \tag{4}$$

where the multidimensional index notation $\boldsymbol{\alpha} = [\alpha_1, \dots, \alpha_M]$ has been adopted. Such a construction guarantees the orthogonality property of the multivariate polynomials, i.e. $\mathbb{E}\left[\psi_{\boldsymbol{\alpha}}(\mathbf{x})\,\psi_{\boldsymbol{\beta}}(\mathbf{x})\right] = \delta_{\boldsymbol{\alpha}\boldsymbol{\beta}}$. In computational applications, the PC expansion in Eq. (1) must be truncated after P terms. A classical approach consists in retaining all those polynomials $\psi_{\boldsymbol{\alpha}}$ with total degree up to p, that is $0 \leq |\boldsymbol{\alpha}| \leq p$, with $|\boldsymbol{\alpha}| = \sum_{i=1}^{M} \alpha_i$. On this basis, the truncated PCE can be written in matrix form as:

$$\mathcal{M}_p(\mathbf{x}) = \sum_{0 \leq |\boldsymbol{\alpha}| \leq p} a_{\boldsymbol{\alpha}} \psi_{\boldsymbol{\alpha}}(\mathbf{x}) = \mathbf{a}^{\mathrm{T}} \boldsymbol{\psi}(\mathbf{x}), \tag{5}$$

where $\mathbf{a}$ and $\boldsymbol{\psi}$ are vectors containing the coefficients $\{a_{\boldsymbol{\alpha}}, 0 \leq |\boldsymbol{\alpha}| \leq p\}$ and the corresponding basis polynomials $\{\psi_{\boldsymbol{\alpha}}, 0 \leq |\boldsymbol{\alpha}| \leq p\}$. The PC coefficients can be estimated by least squares regression. To do so, a set of N realizations $\mathbf{X} = \left[\mathbf{x}^{(1)}, \dots, \mathbf{x}^{(N)}\right]$ of the input random variables are selected in order to cover the design space, also referred to as the experimental design (ED) or training dataset. Accordingly, a set of model realizations/evaluations $\mathbf{Y} = \left[y^{(1)}, \dots, y^{(N)}\right]^{\mathrm{T}}$ is obtained by Monte Carlo simulations (MCS) of the forward model, i.e. $y^{(i)} = \mathcal{M}\left(\mathbf{x}^{(i)}\right)$. Then, the least squares estimate of $\mathbf{a}$ reads:

$$\hat{\mathbf{a}} = \left(\boldsymbol{\Psi}^{\mathrm{T}}\boldsymbol{\Psi}\right)^{-1} \boldsymbol{\Psi}^{\mathrm{T}}\mathbf{Y}, \tag{6}$$

where the components of the data matrix $\mathbf{\Psi}$ are defined as $\mathbf{\Psi}_{ij} = \psi_{\alpha_j}\left(\mathbf{x}^{(i)}\right), i = 1, \ldots, N, j = 0, \ldots, P-1$. The truncation scheme in Eq. (5) leads to a total number of terms in the expansion $\mathcal{A}^{M,p} = \left\{\alpha \in \mathbb{N}^M : 0 \leq |\alpha| \leq p\right\}$:

$$\mathrm{card}\mathcal{A}^{M,p} = \binom{M+p}{p} = \frac{(M+p)!}{M!p!}. \tag{7}$$

In general, any truncation scheme corresponds to a specific choice of a non empty finite set $\mathcal{A}$ of indices $\boldsymbol{\alpha}$. On this basis, it is possible to use the ED to estimate the coefficients of the associated PCE by least squares fitting following Eq. (6), leading to:

$$\hat{\mathcal{M}}_{\mathcal{A}} = \sum_{\alpha \in \mathcal{A}} \hat{a}_\alpha \psi_\alpha(\mathbf{x}) = \hat{\mathbf{a}}^{\mathrm{T}} \boldsymbol{\psi}(\mathbf{x}). \tag{8}$$

The quality of the fitted PCE can be assessed through several error measurements. A common error quantity is the empirical generalization error E_{rr} defined as the mean squared value of the residuals, that is the differences between the model evaluations and the predicted values by the fitted PCE:

$$E_{rr} = \frac{1}{N} \sum_{i=1}^{N} \left[\mathcal{M}(\mathbf{x}) - \hat{\mathcal{M}}_{\mathcal{A}}(\mathbf{x}^{(i)})\right]^2. \tag{9}$$

A key limitation of E_{rr} in Eq. (9) regards its sensitivity to overfitting, which typically leads to underestimates of the generalization error. Indeed, it is clear that E_{rr} systematically decreases as the complexity of the PC expansion in Eq. (5) increases. A better metric for cross-validation applications with less sensitivity to overfitting is the so-called leave-one-out error Err_{LOO} [58]. Let us denote by $\hat{\mathcal{M}}_{\mathcal{A}}^{(-i)}$ the meta-model that has been built from the ED but removing the i-th observation. Then, the predicted residual is defined as the difference between the model evaluation at $\mathbf{x}^{(i)}$ and its prediction by $\hat{\mathcal{M}}_{\mathcal{A}}^{(-i)}$:

$$\Delta^{(i)} = \mathcal{M}(\mathbf{x}^{(i)}) - \hat{\mathcal{M}}_{\mathcal{A}}^{(-i)}(\mathbf{x}^{(i)}), \tag{10}$$

and the leave-one-out error is estimated as:

$$Err_{LOO} = \frac{1}{N} \sum_{i=1}^{N} \left(\Delta^{(i)}\right)^2. \tag{11}$$

The definition in Eq. (11) involves multiple PCE fittings and model evaluations, although within the context of linearly parametrized regression, it is possible to calculate Err_{LOO} analytically [59]:

$$Err_{LOO} = \frac{1}{N} \sum_{i=1}^{N} \left(\frac{\mathcal{M}(x^{(i)}) - \hat{\mathcal{M}}_{\mathcal{A}}(x^{(i)})}{1 - h_i}\right)^2, \tag{12}$$

where

$$h_i = \psi_{A^{(k)}} \left(\psi_{A^{(k)}}^{\mathrm{T}} \psi_{A^{(k)}}\right)^{-1} \psi_{A^{(k)}}^{\mathrm{T}}. \tag{13}$$

The computational cost involved in the fitting of the PCE using the truncation scheme in Eq. (5) may be very high if the number of input variables M or the polynomial degree p are considerably large. Note that, as a rule of thumb, the number of realizations in the ED to uniformly cover the input design space is usually defined as two or three times the cardinality of the expansion, i.e. $\mathrm{card}\mathcal{A}^{M,p}$. An alternative hyperbolic truncation scheme was proposed by Blatman and Sudret [58] to alleviate the computational cost in the PCE. Those authors defined a q-norm, $0 < q < 1$, as:

$$||\boldsymbol{\alpha}||_q = \left(\sum_{i=1}^{M} \alpha_i^q\right)^{1/q}, \tag{14}$$

in such a way that a truncated PCE can be obtained by selecting a finite set of indices $\boldsymbol{\alpha}$ with q-norm less than or equal to p:

$$\mathcal{A}^{M,p,q} = \left\{\boldsymbol{\alpha} \in \mathbb{N}^M : ||\alpha||_q \leq p\right\}. \tag{15}$$

The previous approach reduces the number of terms in the PCE by penalizing high-rank indices and favouring low-order interactions. Nonetheless, the resulting expansion may remain too costly when large-dimensional and highly non-linear problems are to be addressed. In such cases, it is often found that the non-zero coefficients in the expansion form a sparse subset of $\mathcal{A}^{M,p,q}$. This motivates the use of sparse linear regression methods such as the LAR algorithm to further reduce the number of basis polynomials ψ_α in the expansion. LAR is an efficient algorithm for model selection of sparse linear models [53]. In the context of PCE, LAR provides a collection of PC expansions incorporating an increasing number of basis polynomials, from 1 to $P = \operatorname{card}\mathcal{A}^{M,p,q}$. The resulting sequence of index sets $\mathcal{A}^{(k)}$, $k = 0, \ldots, \min(P, N-1)$, is used to construct different PC expansions $\mathcal{M}_{\mathcal{A}^{(k)}}$ and, finally, a cross validation procedure is implemented for selecting the best meta-model. The definition of the optimum PCE using the LAR algorithm involves the following steps [58]:

1. Run the LAR procedure for given degree p and norm q.
   (a) Initialize to zero the polynomial coefficients, i.e. $a_{\alpha 0}, \ldots, a_{\alpha p-1} = 0$. Set the initial residual equal to the vector of observations $\mathbf{Y}$.
   (b) Find the vector $\boldsymbol{\psi}_{\alpha j}$, which is most correlated with the current residual.
   (c) Move $a_{\alpha j}$ from 0 towards the least-square coefficient of the current residual on $\boldsymbol{\psi}_{\alpha j}$, until some other predictor $\boldsymbol{\psi}_{\alpha k}$ has as much correlation with the current residual. Such a move corresponds to the approximation of the active coefficients towards their least-square value, that is $\hat{\mathbf{a}}^{(k+1)} = \hat{\mathbf{a}}^{(k)} + \gamma^{(k)}\tilde{\mathbf{w}}^{(k)}$. Vector $\tilde{\mathbf{w}}^{(k)}$ and coefficient $\gamma^{(k)}$ are referred to as the LAR descent direction and step, respectively. Both quantities may be derived algebraically as shown in [53].
   (d) Continue the procedure until $m = \min(P, N-1)$ basis polynomials have been entered.
2. Recompute the coefficients of each produced sparse meta-model by least-squares regression.
3. Estimate the leave-one-out-error Err_{LOO} in Eq. (12) associated to each meta-model and retain the one with the lowest error estimate.

It was shown in reference [53] that LAR is noticeably efficient since it only requires $O\left(NP^2 + P^3\right)$ computations (i.e. the computational cost of ordinary least-square regression on P predictors) for producing a set of m meta-models. Additionally, in order to select the optimal degree p, the previous LAR approach can be performed for a series of potential degree values within certain interval $p \in [p_{min}, p_{max}]$. After every step in the analysis, the best PC expansion is stored and certain error/quality measurement is computed. Once complete, the optimal PC expansion is chosen as the meta-model with the minimum error/quality measurement. As the quality measurement, a corrected error estimate of the leave-one-out error in Eq. (12) accounting for the number of terms in the PC approximation P and the number of realizations in the ED N is used in this work as:

$$Err^*_{LOO} = Err_{LOO}\, T(P, N), \tag{16}$$

with $T(P, N)$ a correcting factor derived in [60] as:

$$T(P, N) = \frac{N}{N-P}\left[1 + \frac{\operatorname{tr}\left(\mathbf{C}_{emp}^{-1}\right)}{N}\right], \tag{17}$$

where

$$\mathbf{C}_{emp} = \frac{1}{N}\boldsymbol{\Psi}^{\mathrm{T}}\boldsymbol{\Psi}. \tag{18}$$

3.2. PCE-based Kriging interpolation

The universal Kriging model approximates the response of a computational model as a realization of a Gaussian random process as [61]:

$$\hat{\mathcal{M}}(\mathbf{x}) = \mathcal{F}(\mathbf{x}) + \mathcal{Z}(\mathbf{x}), \tag{19}$$

where $\mathcal{F}(\mathbf{x})$ is a regression model, also called trend, and $\mathcal{Z}(\mathbf{x})$ is a zero-mean stochastic process. The latter is fully determined by its covariance function:

$$\operatorname{Cov}\left(\mathcal{Z}(\mathbf{x}), \mathcal{Z}(\mathbf{x}')\right) = \mathbb{E}\left[\mathcal{Z}(\mathbf{x})\mathcal{Z}(\mathbf{x}')\right] = \sigma^2 R\left(\left|\mathbf{x} - \mathbf{x}'\right|; \boldsymbol{\theta}\right), \tag{20}$$

with σ^2 being the Gaussian process variance, and $R(|\mathbf{x} - \mathbf{x}'|; \boldsymbol{\theta})$ an auto-correlation function between two arbitrary input sample points $\mathbf{x}$ and $\mathbf{x}$' and dependent upon certain hyper-parameters $\boldsymbol{\theta}$. The trend term of the universal Kriging model in Eq. (19) approximates the global behaviour of $\mathcal{M}$, while the local variability is captured by the stochastic term. In this work, the trend term is defined as the truncated PC expansion using the LAR procedure introduced in the previous section as:

$$\hat{\mathcal{M}}(\mathbf{x}) = \sum_{\alpha\in\mathcal{A}} \hat{a}_\alpha \psi_\alpha(\mathbf{x}) + \mathcal{Z}(\mathbf{x}) = \mathbf{a}^{\mathrm{T}}\boldsymbol{\psi}(\mathbf{x}) + \mathcal{Z}(\mathbf{x}). \tag{21}$$

Then, the construction of the Kriging meta-model in Eq. (21) consists in the determination of the coefficients of the PC expansion, $\mathbf{a}$, the process variance, σ^2, and the hyper-parameters of the auto-correlation function, $\boldsymbol{\theta}$. In this work, auto-correlation functions are defined as the product of one-dimensional Gaussian correlations in the form [62]:

$$R\left(\mathbf{x}_i, \mathbf{x}_j, \boldsymbol{\theta}\right) = \prod_{k=1}^{M} \exp\left[-\theta_k \left(x_i^{(k)} - x_j^{(k)}\right)^2\right]. \tag{22}$$

Hyper-parameters θ_k in Eq. (22) determine the shape of the correlation function, with larger values of θ_k leading to faster decreases along the k-th dimension of input vector $\mathbf{x}$. This definition allows one to accommodate anisotropic auto-correlations (i.e. different correlations in different directions). Nevertheless, for the sake of simplicity, in this work correlations are assumed isotropic with equal hyper-parameters θ_k across the dimensions of x, i.e. $\theta_k = \theta \quad \forall\, 1 \leq k \leq M$. Given the values of the auto-correlation hyper-parameters $\hat{\boldsymbol{\theta}}$, the calibration of the trend model parameters $\left\{\mathbf{a}\left(\hat{\boldsymbol{\theta}}\right), \sigma^2\left(\hat{\boldsymbol{\theta}}\right)\right\}$ may be computed using an empirical best linear unbiased estimator (BLUE). The optimization yields analytical solutions as functions of $\hat{\boldsymbol{\theta}}$ [61]:

$$\mathbf{a}\left(\hat{\boldsymbol{\theta}}\right) = \left(\mathbf{F}^{\mathrm{T}}\mathbf{R}^{-1}\mathbf{F}\right)^{-1} \mathbf{F}\mathbf{R}^{-1}\mathbf{Y}, \tag{23}$$

$$\sigma^2\left(\hat{\boldsymbol{\theta}}\right) = \frac{1}{N}\left(\mathbf{Y} - \mathbf{F}\mathbf{a}\right)^{\mathrm{T}} \mathbf{R}^{-1}\left(\mathbf{Y} - \mathbf{F}\mathbf{a}\right), \tag{24}$$

where $\mathbf{R}_{ij} = R\left(\left|\mathbf{x}^{(i)} - \mathbf{x}^{(i)}\right|; \hat{\boldsymbol{\theta}}\right)$ and $\mathbf{F}_{ij} = \psi_j\left(\mathbf{x}^{(i)}\right)$ are the autocorrelation and the information matrices, respectively, evaluated at all the samples of the ED.

The optimal correlation parameters $\hat{\boldsymbol{\theta}}$ are typically determined by either the maximum-likelihood-estimated (labelled with ML) or by the leave-one-out cross validation (labelled with CV) [56], which lead to the following minimization problems:

$$\hat{\boldsymbol{\theta}}_{ML} = \arg\min_{\boldsymbol{\theta}} \left[\frac{1}{N}\left(\mathbf{Y} - \mathbf{F}\mathbf{a}\right)^{\mathrm{T}} \mathbf{R}^{-1}\left(\mathbf{Y} - \mathbf{F}\mathbf{a}\right)\left(\det \mathbf{R}\right)^{1/N}\right], \tag{25}$$

$$\hat{\boldsymbol{\theta}}_{CV} = \arg\min_{\boldsymbol{\theta}} \left[\mathbf{Y}^{\mathrm{T}}\mathbf{R}^{-1}\mathrm{diag}\left(\mathbf{R}^{-1}\right)^{-2}\mathbf{R}^{-1}\mathbf{Y}\right]. \tag{26}$$

Determining the optimal correlation parameters in Eqs. (25) and (26) is a complex multi-dimensional minimization problem. In order to prevent the solution from depending upon initial guesses on the hyper-parameters, a global optimization approach based on GA has been implemented in this work. Once the optimal model parameters are determined, the prediction of a new point $\mathbf{x}$ is given by a Gaussian random variable with mean $\mu(\mathbf{x})$ and variance $\sigma^2(\mathbf{x})$:

$$\mu(\mathbf{x}) = \mathbf{a}^{\mathrm{T}}\boldsymbol{\psi}(\mathbf{x}) + \mathbf{r}(\mathbf{x})^{\mathrm{T}}\mathbf{R}^{-1}\left(\mathbf{Y} - \mathbf{F}\mathbf{a}\right), \tag{27}$$

$$\sigma^2(\mathbf{x}) = \sigma^2\left(1 - \left\langle \boldsymbol{\psi}(\mathbf{x})^{\mathrm{T}}\mathbf{r}(\mathbf{x})^{\mathrm{T}}\right\rangle \begin{bmatrix} \mathbf{0} & \mathbf{F}^{\mathrm{T}} \\ \mathbf{F} & \mathbf{R} \end{bmatrix} \begin{bmatrix} \boldsymbol{\psi}(\mathbf{x}) \\ \mathbf{r}(\mathbf{x}) \end{bmatrix}\right), \tag{28}$$

where $r_i(\mathbf{x}) = R\left(\left|\mathbf{x} - \mathbf{x}^{(i)}\right|; \boldsymbol{\theta}\right)$ is the correlation between the new sample $\mathbf{x}$ and the sample $\mathbf{x}^{(i)}$ of the ED. The prediction error mean is used as the surrogate to the original model $\mathcal{M}$, whereas the variance gives a local error indicator about the precision. It is important to note that the Kriging model perfectly interpolates the data of the ED, i. e. $\hat{\mathcal{M}}(\mathbf{x}^{(i)}) = \mathcal{M}(\mathbf{x}^{(i)})$, $\forall \mathbf{x}^{(i)} \in \mathbf{X}$.

4. Surrogate model-based Bayesian model updating

Once the previous PC-Kriging surrogate model is constructed, it is used to continuously infer the model parameters $\mathbf{x}$ conditional on a set of experimentally identified modal properties $\mathbf{d}(t) \in \mathbb{R}^{m(1+N_o)}$. The modal data in $\mathbf{d}(t)$ comprise periodically identified resonant frequencies $f_r(t)$ and mode shapes $\boldsymbol{\varphi}_r(t) \in \mathbb{R}^{N_o}$ at time instants t, with m and N_o being the number of identified modes and measured degrees of freedom (DOFs), respectively. The Bayes' theorem is used to estimate the posterior distribution $p\left(\mathbf{x}(t)|\,\mathbf{d}(t),\widehat{\mathcal{M}}\right)$ of the model parameters $\mathbf{x}(t)$ at time instants t given the surrogate model $\widehat{\mathcal{M}}$ as:

$$p\left(\mathbf{x}(t)|\,\mathbf{d}(t),\widehat{\mathcal{M}}\right) = \frac{p\left(\mathbf{d}(t)|\,\mathbf{x}(t),\widehat{\mathcal{M}}\right)p\left(\mathbf{x}(t)|\,\widehat{\mathcal{M}}\right)}{p\left(\mathbf{d}(t)|\,\widehat{\mathcal{M}}\right)}, \tag{29}$$

where $p\left(\mathbf{x}(t)|\,\widehat{\mathcal{M}}\right)$ is the prior distribution of the model parameters, $p\left(\mathbf{d}(t)|\,\mathbf{x}(t),\widehat{\mathcal{M}}\right)$ denotes the likelihood function, and $p\left(\mathbf{d}(t)|\,\widehat{\mathcal{M}}\right)$ stands for the evidence of the model class, selected so that $p\left(\mathbf{x}(t)|\,\mathbf{d}(t),\widehat{\mathcal{M}}\right)$ integrates to one. For clarity of the notation, the dependence on time t is dropped in the following formulation and, since only a surrogate model is used, specific reference to the model class $\widehat{\mathcal{M}}$ is also omitted.

The likelihood function $p(\mathbf{d}\,|\,\mathbf{x})$ represents the probability of observing the measured data $\mathbf{d}$ for model parameters equal to $\mathbf{x}$. Its definition is of pivotal importance in Bayesian inference, since it determines the probabilistic relation between the model predictions and experimental data including the unavoidable model and measurement errors. For modal frequencies, the most common approach to represent the likelihood function is the uncorrelated Gaussian error assumption for each identified modal frequency (see e.g. [38, 45]):

$$f_r = \hat{f}_r(\mathbf{x}) + \varepsilon_{f_r}, \tag{30}$$

where $\hat{f}_r(\mathbf{x})$ is the PC-kriging model prediction, while ε_{f_r} is the prediction error for the r-th modal frequency taken to be Gaussian with zero mean and standard deviation σ_{f_r}. Then, the likelihood term of the r-th resonant frequency reads:

$$p(f_r\,|\,\mathbf{x}) = \frac{1}{\sigma_{f_r}\sqrt{2\pi}}\exp\left\{-\frac{1}{2}\frac{\left(f_r - \hat{f}_r(\mathbf{x})\right)^2}{\sigma_{f_r}^2}\right\}. \tag{31}$$

With regard to the mode shapes, an often-used formulation is to assume that the discrepancy vector between the measured mode shape vector and the model predicted one follows a zero-mean multivariate Gaussian distribution [51, 63]. The prediction error equation for the r-th mode shape is then:

$$\boldsymbol{\varphi}_r = \beta_r(\mathbf{x})\widehat{\boldsymbol{\varphi}}_r(\mathbf{x}) + \boldsymbol{\varepsilon}_{\varphi_r}, \tag{32}$$

where $\boldsymbol{\varepsilon}_{\varphi_r}$ is the prediction error vector for the r-th mode shape taken to be Gaussian with zero mean and covariance matrix $\sigma_{\varphi_r}^2\boldsymbol{\Sigma}_{\varphi_r}$, where matrix $\boldsymbol{\Sigma}_{\varphi_r}$ specifies the possible correlation between the components of the prediction error of the r-th mode shape. Term $\beta_r(\mathbf{x})$ is a normalization constant to accommodate the different normalizations of the experimental mode shapes $\boldsymbol{\varphi}_r$ (normalized to unit Euclidean norm) and the model predicted ones $\widehat{\boldsymbol{\varphi}}_r(\mathbf{x})$ (often mass-normalized). The scalar $\beta_r(\mathbf{x})$ is determined as the least squares solution of $\left\|\boldsymbol{\varphi}_r - \beta_r(\mathbf{x})\widehat{\boldsymbol{\varphi}}_r(\mathbf{x})\right\| = \mathbf{0}$, with $\|\cdot\|$ denoting Euclidean norm. This leads to:

$$\beta_r(\mathbf{x}) = \frac{\boldsymbol{\varphi}_r^{\mathrm{T}}\widehat{\boldsymbol{\varphi}}_r(\mathbf{x})}{\widehat{\boldsymbol{\varphi}}_r(\mathbf{x})^{\mathrm{T}}\widehat{\boldsymbol{\varphi}}_r(\mathbf{x})}. \tag{33}$$

The definition of the covariance matrix $\boldsymbol{\Sigma}_{\varphi_r}$ may be challenging in practice. For simplicity, the mode shape prediction error vectors are assumed uncorrelated in this work, whereby the covariance matrix simplifies to a diagonal matrix:

$$\boldsymbol{\Sigma}_{\varphi_r} = \frac{\boldsymbol{\varphi}_r^{\mathrm{T}}\boldsymbol{\varphi}_r}{N_0}\mathbf{I}_{N_0}, \tag{34}$$

with $\mathbf{I}_{N_0}$ being the $N_0 \times N_0$ identity matrix. In this way, the likelihood term of the r-th mode shape reads:

$$p(\boldsymbol{\varphi}_r\,|\,\mathbf{x}) = \frac{\exp\left\{-\frac{1}{2}\left[\boldsymbol{\varphi}_r - \beta_r(\mathbf{x})\boldsymbol{\varphi}_r(\mathbf{x})\right]^{\mathrm{T}}\boldsymbol{\Sigma}_{\varphi_r}^{-1}\left[\boldsymbol{\varphi}_r - \beta_r(\mathbf{x})\boldsymbol{\varphi}_r(\mathbf{x})\right]\right\}}{\sqrt{(2\pi)^{N_0}\det\left|\boldsymbol{\Sigma}_{\varphi_r}\right|}}. \tag{35}$$

In order to limit the number of parameters in the inference, a common approach in the literature consists of considering equal prediction errors σ_{f_r} and σ_{φ_r} for all the modes (see e.g. [27, 63, 64]) as a trade-off between computational burden and accuracy. Therefore, the dependence of prediction errors on r is dropped hereafter. Alternatively, the likelihood term of the r-th mode shape can be expressed using Modal Assurance Criterion (MAC) values. The MAC value measures the similarity between the experimental and model predicted mode shapes as:

$$\mathrm{MAC}_r = \frac{\left|\boldsymbol{\varphi}_r^{\mathrm{T}} \widehat{\boldsymbol{\varphi}}_r(\mathbf{x})\right|^2}{\left(\boldsymbol{\varphi}_r^{\mathrm{T}}\, \boldsymbol{\varphi}_r\right) \left(\widehat{\boldsymbol{\varphi}}_r(\mathbf{x})^{\mathrm{T}}\, \widehat{\boldsymbol{\varphi}}_r(\mathbf{x})\right)}, \tag{36}$$

and spans between 0 and 1. A value of 0 implies that the modes do not show any correlation, whereas a value of 1 indicates absolute correlation. Taking the square root of (1-MAC) gives the fractional error between the measured and calculated mode shapes, i.e. $\varepsilon_{ms} = (1 - \mathrm{MAC}_r)^{1/2}$. Assuming the mode shape fractional error ε_{ms} follows a zero-mean Gaussian distribution, the PDF of the mode shapes in terms of MAC values can be written as [65]:

$$p\left(\boldsymbol{\varphi}_r \,|\, \mathbf{x}\right) = \frac{1}{\sqrt{2\pi\sigma_{\varphi}^2}} \exp\left\{-\frac{1}{2\sigma_{\varphi}^2}\left(1 - \mathrm{MAC}_r\right)\right\}. \tag{37}$$

On this basis, assuming the errors independence, the total likelihood function can be easily calculated as the product of the individual likelihoods. Considering that m modes of vibration have been identified, the total likelihood function reads:

$$p\left(\mathbf{d} \,|\, \boldsymbol{\theta}\right) = \prod_{r=1}^{m} p\left(f_r \,|\, \boldsymbol{\theta}\right) p\left(\boldsymbol{\varphi}_r \,|\, \boldsymbol{\theta}\right), \tag{38}$$

where the parameter set $\boldsymbol{\theta}$ includes the model parameters $\mathbf{x}$ and the standard deviations σ_f and σ_{φ}. Note that the error uncertainties are unknown in reality, being necessary to make assumptions on their initial values. To do so, different methodologies have been proposed in the literature, including the posterior variance of the modal features estimated by Bayesian OMA, coefficients of variations of identified modal properties [51], or based on users' intuition and experience [64].

The evaluation in closed-form of the posterior PDF in Eq. (29) is infeasible in most applications, so an adaptive MCMC sampling method is implemented herein. The adopted MCMC strategy, named DRAM and firstly proposed by Haario *et al.* [66], combines DR with an AM algorithm. In this work, the DRAM algorithm with one delayed rejection step has been implemented according to the following steps:

1. Choose the length of the chain N_c and initialize the parameter set $\boldsymbol{\theta}_c = \boldsymbol{\theta}_0$, the error variances $\sigma_{f_0}^2$ and $\sigma_{\varphi_0}^2$, and the covariance of the proposal distribution $\Sigma_p = \Sigma_0$. Select the initial non-adaptation period n_a and set $i = 1$.

2. Propose a new parameter value $\boldsymbol{\theta}_{p,1}$ by sampling from a proposal Gaussian distribution $S(\boldsymbol{\theta}, \boldsymbol{\theta}_c)$ with mean at the current point $\boldsymbol{\theta}_c$ and covariance Σ_p, i.e. $\boldsymbol{\theta}_{p,1} = \boldsymbol{\theta}_c + \xi$, with $\xi \sim \mathcal{N}\left(\mathbf{0}, \Sigma_p\right)$.

3. Compute the acceptance probability:

$$\alpha_1\left(\boldsymbol{\theta}_c, \boldsymbol{\theta}_{p,1}\right) = \min\left(1, \frac{p\left(\boldsymbol{\theta}_{p,1} \,\middle|\, \mathbf{d}\right) S\left(\boldsymbol{\theta}_{p,1}, \boldsymbol{\theta}_c\right)}{p\left(\boldsymbol{\theta}_c \,|\, \mathbf{d}\right) S\left(\boldsymbol{\theta}_c, \boldsymbol{\theta}_{p,1}\right)}\right). \tag{39}$$

4. Generate a random number $\vartheta \sim \mathcal{U}(0, 1)$. If $\alpha_1\left(\boldsymbol{\theta}_c, \boldsymbol{\theta}_{p,1}\right) > \vartheta$, accept the candidate sample $\boldsymbol{\theta}_i = \boldsymbol{\theta}_{p,1}$ and move to step (8). Otherwise, propose a second stage move in step (5).

5. Propose a second stage move $\boldsymbol{\theta}_{p,2}$ sampling from $S_2(\boldsymbol{\theta}, \boldsymbol{\theta}_{p,1}, \boldsymbol{\theta}_c)$. This second stage proposal is allowed to depend not only on the current position of the chain, but also on the candidate that has just been proposed and rejected. In this work, the covariance of the proposal in the second stage proposal is scaled by a factor γ as $\gamma\Sigma_p$.

6. Compute the acceptance probability

$$\alpha_2\left(\boldsymbol{\theta}_c, \boldsymbol{\theta}_{p,1}, \boldsymbol{\theta}_{p,2}\right) = \min\left\{1, \frac{p\left(\boldsymbol{\theta}_{p,2} \,\middle|\, \mathbf{d}\right) S_1\left(\boldsymbol{\theta}_{p,2}, \boldsymbol{\theta}_{p,1}\right) S_2\left(\boldsymbol{\theta}_{p,2}, \boldsymbol{\theta}_{p,1}, \boldsymbol{\theta}_c\right)\left[1 - \alpha_1\left(\boldsymbol{\theta}_{p,2}, \boldsymbol{\theta}_{p,1}\right)\right]}{p\left(\boldsymbol{\theta}_c \,|\, \mathbf{d}\right) S_1\left(\boldsymbol{\theta}_c, \boldsymbol{\theta}_{p,1}\right) S_2\left(\boldsymbol{\theta}_c, \boldsymbol{\theta}_{p,1}, \boldsymbol{\theta}_{p,1}\right)\left[1 - \alpha_1\left(\boldsymbol{\theta}_c, \boldsymbol{\theta}_{p,1}\right)\right]}\right\}. \tag{40}$$

7. Accept of reject $\boldsymbol{\theta}_{p,2}$ by setting:

$$\boldsymbol{\theta}_i = \begin{cases} \boldsymbol{\theta}_{p,2}, & \text{with probability } \alpha_2\left(\boldsymbol{\theta}_c, \boldsymbol{\theta}_{p,1}, \boldsymbol{\theta}_{p,2}\right), \\ \boldsymbol{\theta}_c, & \text{with probability } 1-\alpha_2\left(\boldsymbol{\theta}_c, \boldsymbol{\theta}_{p,1}, \boldsymbol{\theta}_{p,2}\right), \end{cases} \tag{41}$$

8. Update the error variances $\sigma^2_{f_i}$ and $\sigma^2_{\boldsymbol{\varphi}_i}$. Assuming an inverse Gamma $\left(\Gamma^{-1}\right)$ prior distribution for the error variances, the conjugate posterior also follows an inverse Gamma distribution and new samples can be drawn following a standard Gibbs sampling procedure [67]:

$$p\left(\sigma^2_f \middle| \boldsymbol{\theta}_i, \mathbf{d}\right) \sim \Gamma^{-1}\left(\frac{n_{o,f}+m}{2}, \frac{n_{o,f}\, S^2_{o,f} + SS_f\left(\boldsymbol{\theta}_i\right)}{2}\right), \tag{42}$$

$$p\left(\sigma^2_{\boldsymbol{\varphi}} \middle| \boldsymbol{\theta}_i, \mathbf{d}\right) \sim \Gamma^{-1}\left(\frac{n_{o,\boldsymbol{\varphi}}+m}{2}, \frac{n_{o,\boldsymbol{\varphi}}\, S^2_{o,\boldsymbol{\varphi}} + SS_{\boldsymbol{\varphi}}\left(\boldsymbol{\theta}_i\right)}{2}\right), \tag{43}$$

where $n_{o,f}$, $n_{o,\boldsymbol{\varphi}}$, $S_{o,f}$ and $S_{o,\boldsymbol{\varphi}}$ are the input parameters of the prior distributions of σ^2_f and $\sigma^2_{\boldsymbol{\varphi}}$. In this work, the following values are chosen with the aim of making the priors uniformative: $n_{o,f} = n_{o,\boldsymbol{\varphi}} = 1$ and $S_{o,f} = \sigma^2_{f_0}$, $S_{o,\boldsymbol{\varphi}} = \sigma^2_{\boldsymbol{\varphi}_0}$. Terms $SS_f\left(\boldsymbol{\theta}_i\right)$ and $SS_{\boldsymbol{\varphi}}\left(\boldsymbol{\theta}_i\right)$ denote the sum of squared errors of resonant frequencies and mode shapes given by:

$$SS_f\left(\boldsymbol{\theta}_i\right) = \sum_{r=1}^{m}\left(f_r - f_r\left(\boldsymbol{\theta}_i\right)\right)^2, \tag{44}$$

$$SS_{\boldsymbol{\varphi}}\left(\boldsymbol{\theta}_i\right) = \sum_{r=1}^{m}\frac{N_0}{\boldsymbol{\varphi}_r^{\mathrm{T}}\boldsymbol{\varphi}_r}\left[\boldsymbol{\varphi}_r - \beta_r(\boldsymbol{\theta}_i)\boldsymbol{\varphi}_r(\boldsymbol{\theta}_i)\right]^{\mathrm{T}}\left[\boldsymbol{\varphi}_r - \beta_r(\boldsymbol{\theta}_i)\boldsymbol{\varphi}_r(\boldsymbol{\theta}_i)\right]. \tag{45}$$

9. Update the covariance matrix Σ_p as:

$$\Sigma_p = \begin{cases} \Sigma_0 & i \le n_a \\ s_d \operatorname{cov}\left(\boldsymbol{\theta}_1, \ldots, \boldsymbol{\theta}_i\right) & i > n_a \end{cases} \tag{46}$$

with $s_d = 2.4^2/d$ a scaling parameter, with d being the number of fitting parameters [66].

10. Set $i = i + 1$ and go to step 2 until the desired number of samples N_c is obtained.

5. Numerical results and discussion

The effectiveness of the proposed surrogate model-based damage identification approach is evaluated through three case studies. These firstly include a toy example of an analytical function in Section 5.1, and a numerically simulated truss structure in Section 5.2. The first case study is intended to demonstrate the accuracy and robustness of the proposed surrogate model. On the other hand, the second case study analyses the effectiveness of the developed surrogate model-based BMU approach for damage identification. Finally, the application of the proposed approach is illustrated with a real case study of a historical masonry tower equipped with a long-term SHM system in Section 5.3 in order to demonstrate the feasibility of the proposed method for real-time full-scale applications.

5.1. Case Study I: Ishigami function

The Ishigami function is a highly non-linear three-dimensional function widely used for benchmarking in uncertainty and sensitivity analysis. It is defined as [68]:

$$y(x_1, x_2, x_3) = \sin x_1 + 7\sin^2 x_2 + 0.1 x_3^4 \sin x_1, \tag{47}$$

where x_i are i.i.d. uniform random variables in $[-\pi, \pi]$.

Numerical results are first presented to compare the effectiveness of the developed PCE-Kriging meta-model with standard sparse PCE and Kriging. To do so, different EDs with increasing sizes N varying from 20 to 300 are generated by Latin-hypercube sampling (LHS). The PCE-Kriging and PCE meta-models are generated considering an orthonormal basis of Legendre polynomials and a q-norm of 0.8. The order of the expansions is defined from

1 to 10 and the leave-one-out error in Eq. (16) is used to select the optimal expansions. The PCE-Kriging meta-models are constructed considering the leave-one-out cross validation objective function given by Eq. (25), and the regression model used for the standard Kriging meta-models is defined using second order polynomial functions. In order to evaluate the uncertainty in the fittings, 100 independent runs per training sample size are considered. The reliability and accuracy of the surrogate models are evaluated by comparing their predictions with the exact solutions of an independent validation set (VS) of VS = 10E+3 samples. In this case study, such a comparison is conducted through the following relative mean squared error (MSE_r):

$$MSE_r = \frac{\sum_{i=1}^{VS} \left[y(x^{(i)}) - \hat{y}(x^{(i)}) \right]^2}{\sum_{i=1}^{VS} \left[y(x^{(i)}) - \bar{y} \right]^2}, \tag{48}$$

where $\bar{y}$ is the analytical mean of the output variable. On this basis, the box plots in Fig. 2 (a) report the MSE_r values obtained for Kriging, PCE, PCE-Kriging. In general, it is observed that standard Kriging yields the largest errors and a slow convergence rate. Conversely, PCE and PCE-Kriging showed a similar performance, with slightly lower errors in the latter in terms of median values. For these models, a sharp decrease from 10^{-4} to 10^{-7} is found for EDs with sample sizes above 50. A similar convergence trend is found in terms of the number of principle terms and the level of sparsity of the PC expansions as reported in Figs. 2 (b) and (c), respectively. Note in Fig. 2 (b) that, although the number of terms involved in the full PC expansion amounts to $\binom{10+3}{3} = 286$, convergence in the sparse PC expansions is achieved for a total number of terms below 30, which corresponds to a sparsity ratio of about 10% (≈30/286). The resulting predictions of the Ishigami function in the VS by the meta-models trained with an ED of 100 samples is shown in Fig. 3. Specifically, Fig. 3 (a) furnishes a scatter plot of the predictions by the meta-models versus the exact solution. This sort of representations allows one to readily assess the reliability of surrogate models by quantifying the dispersion (i.e. prediction errors) along the diagonal line, which represents the perfect regression. In this case, the large scatter of the data-points obtained using standard Kriging confirms the superior performance of PCE and PCE-Kriging, which approximate the perfect model (diagonal line) with coefficients of determination R^2 very close to 1. To illustrate the close agreements found between the analytical function and the predictions by PCE-Kriging, Fig. 3 (b) shows a sample surf plot of the Ishigami function obtained for $x_3 = 1$ and the corresponding predictions of the meta-model with blue scatter points. It is noted in Fig. 3 (c) that the meta-model achieves almost perfect fittings in all the domain, and only slight discrepancies can be observed at the boundaries of x_1 and x_2

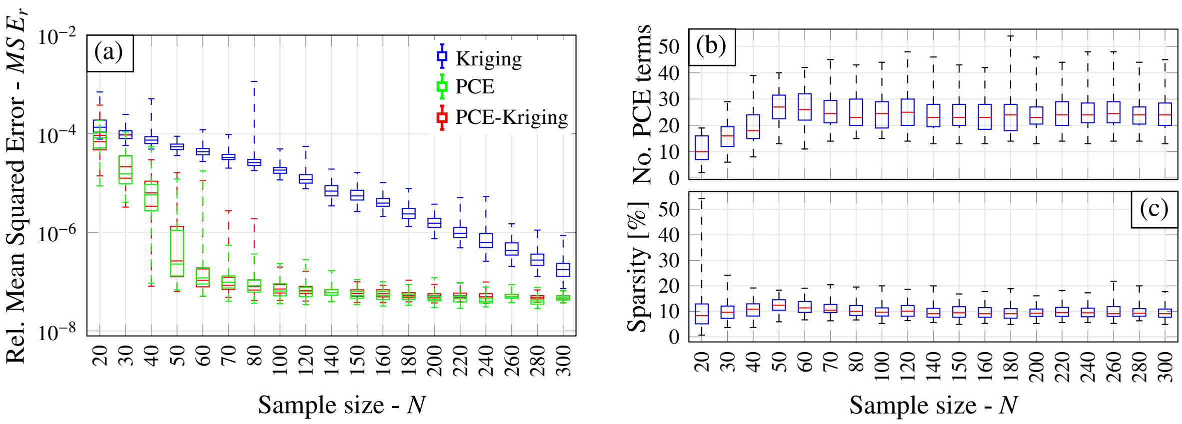

Figure 2: Regression error results for the Ishigami function: (a) global regression error, (b) number of terms in the sparse model, and (c) sparsity level.

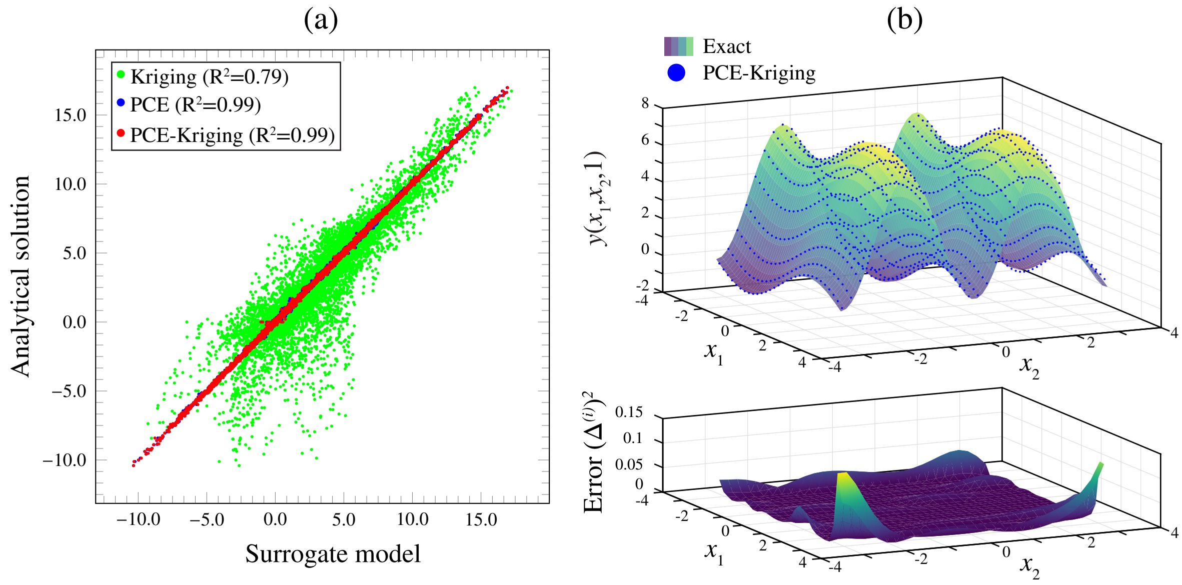

Figure 3: Scatter plot of the predictions of the validation set (10E+3 samples) of the Ishigami function obtained by Kriging, PCE, and PCE-Kriging trained with an ED of 100 samples (a), comparison example between the analytical solution $y(x_1, x_2, 1)$ and the predictions obtained by PCE-Kriging (b) and corresponding squared errors (c).

5.2. *Case Study II: Planar truss structure*

This second case study analyses a simple 31-bar planar truss structure used as a benchmark in many research works on FEM updating (e.g. [69]). The aim of this second case study is to examine the effectiveness of the presented surrogate model-based BMU approach to deal with ill-conditioning and its robustness to noise pollution in the measurements. The geometry and boundary conditions of the structure are shown in Fig. 4. It has been discretized in Matlab using planar 2-D truss elements with two translational DOFs per node, and the material has been considered as linear elastic with Young's modulus $E = 70$ GPa and mass density $\rho = 770$ kg/m^3. In this case study, the elastic moduli of the bars numbered with 31, 1, 28, 4, 18, 14, 7 and 22 are defined as the model updating parameters in $\boldsymbol{\theta}$. Specifically, i.i.d. stiffness multipliers θ_i, $i = 1, \ldots, 8$, uniformly distributed in $[0.7, 1.1]$, are defined as the unknown parameters. The first eight resonant frequencies and mode shapes are taken into account in the subsequent inference analysis. The mode shapes are discretized considering that seven sensors aligned in the vertical direction are located at nodes N2, N4, N6, N8, N10, N12 and N12 (indicated with red arrows in Fig. 4). In the first place, a PCE-Kriging meta-model is generated to reproduce both the natural frequencies and mode shapes, which amounts to a total of 64 univariate surrogate models (eight resonant frequencies plus $8 \cdot 7$ modal components). Legendre polynomials of orders ranging from 1 to 6 are chosen to build the PCE orthonormal basis with a q-norm of 0.6, and the leave-one-out error is used to select the optimal expansions. From preliminary convergence analyses of the statistical distribution of the modal properties of the structure, an ED of $N = 256$ samples drawn using LHS has been selected. To evaluate the accuracy of the constructed surrogate model, a validation set of $VS = 1024$ samples has been defined. In addition, to provide a compact metric of the accuracy of the fittings of the mode shape, a cost function $J_{MAC,r}$ representing the median value of the 1-MAC values between the r-th exact mode shapes $\boldsymbol{\varphi}_r$ and the predictions by the surrogate model $\hat{\boldsymbol{\varphi}}_r(\boldsymbol{\theta})$ in the validation set is introduced as:

$$J_{MAC,r} = \mathrm{med}\left[1 - MAC\left(\boldsymbol{\varphi}_r, \hat{\boldsymbol{\varphi}}_r(\boldsymbol{\theta})\right)\right]. \tag{49}$$

The resulting scatter plots of the exact resonant frequencies and the predictions by the surrogate model are shown in Fig. 5. The low scatter of the points around the diagonal line corroborates that the surrogate models are formed with accuracy, achieving coefficients of determination above 0.99. In addition, very close fittings of the mode shapes have been also obtained, with maximum $J_{MAC,r}$ metric values of the order of E-5. These results demonstrate the accuracy of the developed surrogate model when handling a large number of design variables and moderate to large variation ranges.

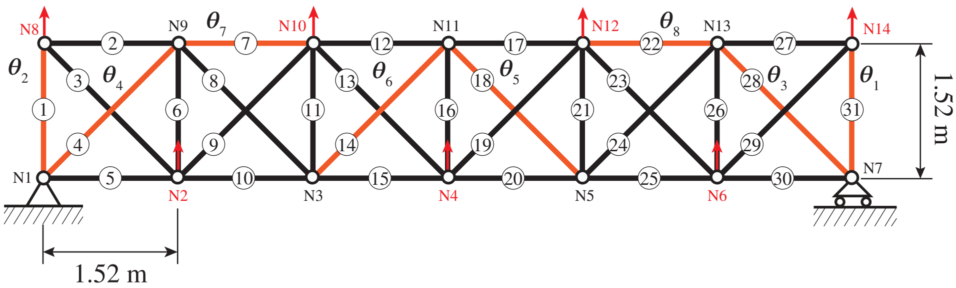

Figure 4: Geometry, boundary conditions and parametrization of the benchmark 31-bar planar truss structure.

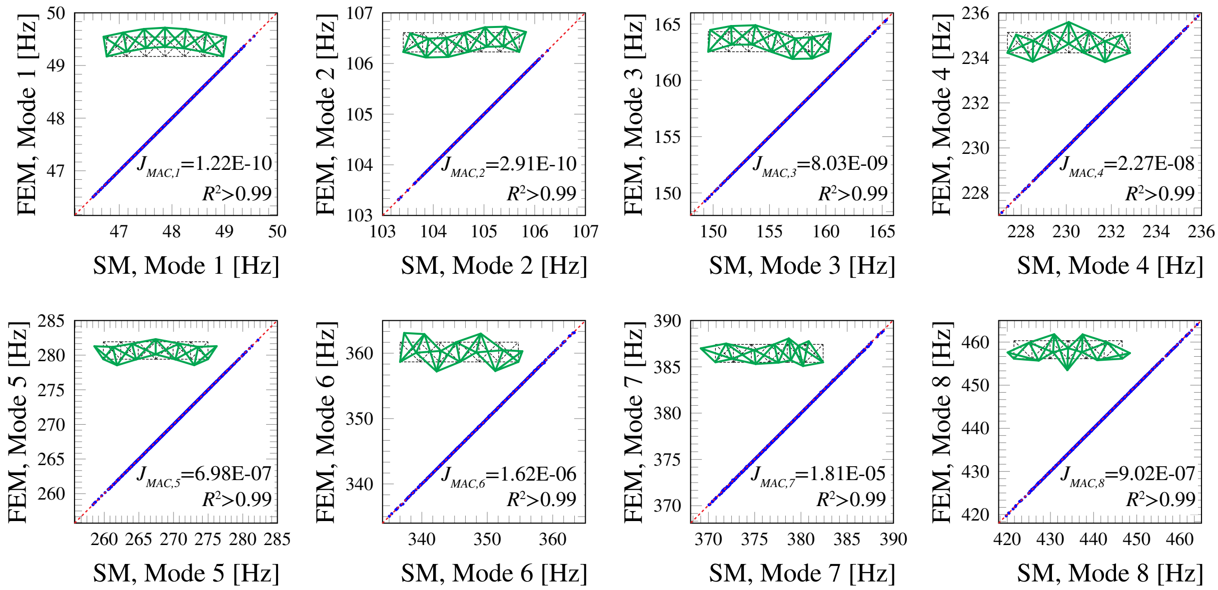

Figure 5: Scatter plot of the PCE-Kriging meta-model (256 training samples) with respect to the FEM of the 31-bar planar truss structure for the first eight natural modes (validation set of 1024 samples).

Once the surrogate model has been proved to accurately reproduce the modal signatures of the truss structure, the BMU approach presented in Section 5 is applied. In these analyses, the likelihood functions reported in Eqs. (33) and (35) are implemented. Considering that the prediction error parameters are the same for all the considered modes, the number of uncertain parameters to be included in the inference amount to 10, i.e. θ_i, $i = 1, \ldots, 8$, σ_f and σ_φ. To illustrate the effectiveness of the implemented adaptive MCMC algorithm, a first analysis considering only θ_1 and θ_2 as the uncertain parameters is presented in Fig. 6. Defining the exact values of $\theta_1 = 0.8$ and $\theta_2 = 1.0$, the Bayesian inference results considering only the resonant frequencies and both the resonant frequencies and mode shapes are presented in Fig. 6 (a) and (b), respectively. The joint PDF of the uncertain parameters is obtained by drawing 8000 Markov chain samples with a burning time of 900 samples. The adaptive MCMC algorithm is activated after the first 1000 samples. The Gaussian proposal is initially defined as a diagonal covariance matrix of value 1E-2 and scaled by the factor $s_d = 2.4^2/d$. In the DR step, the covariance matrix of the proposal distribution is scaled down by a factor $\gamma = 0.1$. The initial location state θ_0 is defined by considering all the uncertain parameters equal to 1.0. To evaluate the effectiveness of the inference of the prediction errors according to Eqs. (42) and (43), large initial values are selected as $\sigma_f^2 = 3\%$ and $\sigma_\varphi^2 = 0.5\%$ (Eq. (35)). The selected hyperparameters led to an average acceptance rate of 67%, which is within the reasonable interval [60% – 70%]. Note that parameters θ_1 and θ_2 correspond to the stiffness multipliers of the symmetric vertical bars 31 and 1. Therefore, the problem becomes ill-posed when only the resonant frequencies are included in the inference, and two potential solutions arise, namely $(\theta_1, \theta_2) = (0.8, 1.0)$ and $(\theta_1, \theta_2) = (1.0, 0.8)$. It is observed in Fig. 6 that, indeed, the implemented DRAM algorithm is capable of finding the two solutions, leading to a bimodal PDF. It is evidenced in the Markov chain shown in Fig. 6 (a) how the adaptive MCMC algorithm allows exploring the two modes in the distribution, without getting stuck around as usual when implementing standard MCMC methods. Conversely, when both natural frequencies and mode shapes are included in the inference, the identification is well-posed and the resulting PDF becomes unimodal with one single mode at the true solution. In addition, it is observed that the marginal chains of the prediction errors rapidly achieve convergence, reaching low mean values and dispersion as expected given that the model has been used to generate the pseudo-experimental values.

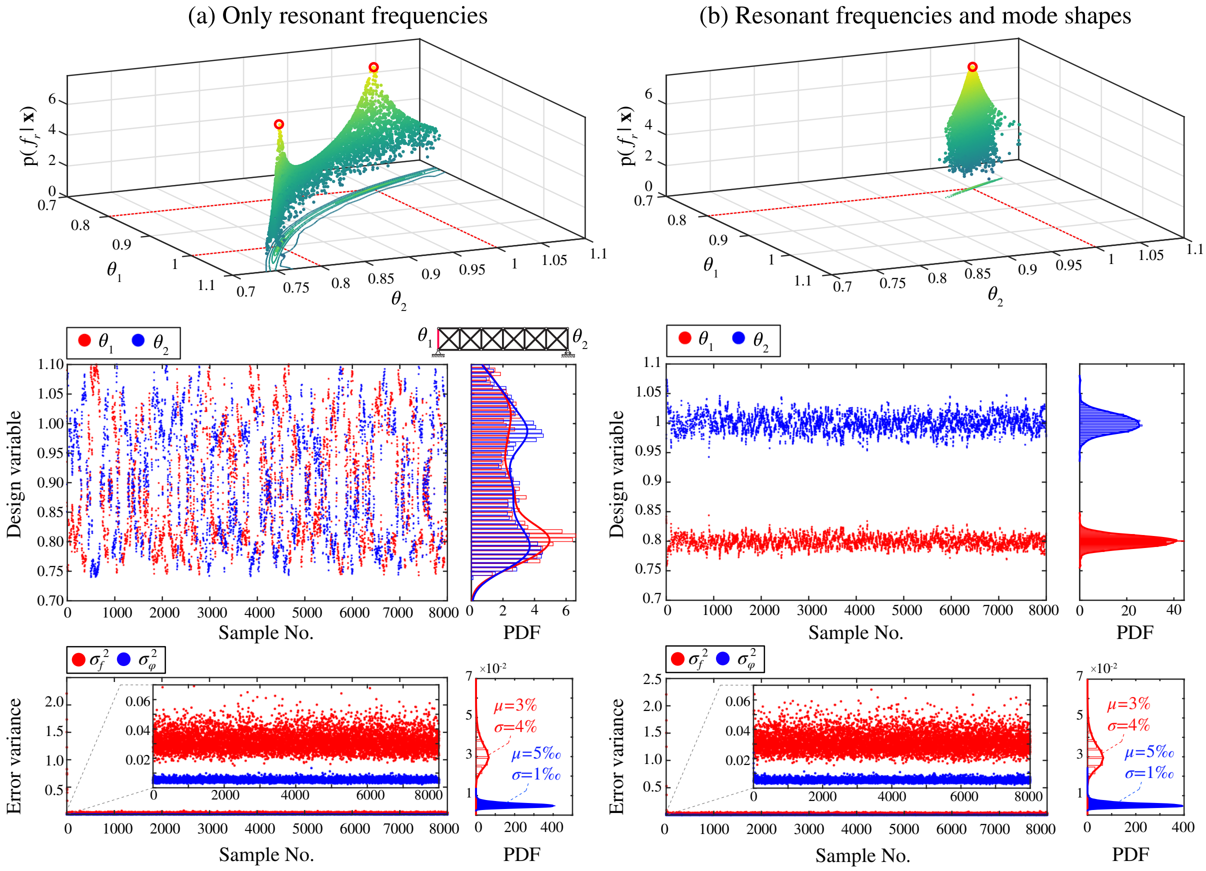

Figure 6: Bayesian inference results of the stiffness multipliers θ_1 and θ_2 of the end verticals of the 31-bar truss structure and error variances considering: (a) resonant frequencies, (b) resonant frequencies and mode shapes. True solution: $(\theta_1, \theta_2) = (0.8, 1.0)$.

Finally, the Bayesian inference results considering 10 unknown parameters are reported in Table 1. The assigned exact values of the stiffness parameters θ_i, $i = 1, \ldots, 8$, are given in the second column, and the model specified by those values is regarded as the reference model. The first eight frequencies and modal vectors at the five observation points compose the simulated measurement data. In these analyses, a total number of 1000 samples are drawn by the previously introduced BMU. The rest of the hyperparameters are kept from the previous analysis. The robustness and reliability of the presented algorithm for model updating in the presence of noise in the identified modal signatures are tested herein. To do so, the simulated modal properties have been corrupted with Gaussian white noise at different levels as $f_r^n = f_r(1 + \eta_1)$ and $\varphi_{r,i}^n = \varphi_{r,i}[1 + \eta_2 \mathrm{std}(\boldsymbol{\varphi}_r)]$. Terms f_r^n and $\varphi_{r,i}^n$ denote the noisy r-th natural frequency and the i-th component of the r-th mode shape, respectively, while η_1 and η_2 are zero-mean Gaussian processes. On this basis, two different noise levels have been considered, including: Noise level 1: $\eta_1 \sim \mathcal{N}(\mu = 0, \sigma = 1E-2)$ and $\eta_2 \sim \mathcal{N}(\mu = 0, \sigma = 1E-1)$; Noise level 2: $\eta_1 \sim \mathcal{N}(\mu = 0, \sigma = 5E-2)$ and $\eta_2 \sim \mathcal{N}(\mu = 0, \sigma = 5E-1)$; and Noise level 3: $\eta_3 \sim \mathcal{N}(\mu = 0, \sigma = 1E-1)$ and $\eta_2 \sim \mathcal{N}(\mu = 0, \sigma = 1E+0)$. This noise model was considered to be consistent with typical measurement conditions, in which mode shape measurements often exhibit an order-of-magnitude lower precision. For each noise level, 30 realizations are carried out and the sample means of the obtained Markov chains and the relative estimation errors of the unknown structural parameters with respect to the exact values are presented in Table 1. It is noted that the updated parameters have close agreements with the assigned exact values for the first two noise levels, with mean absolute relative errors of 5.14%, 5.50% for noise levels 1, and 2, respectively. Errors start to increase considerably only for the third noise level, which represents a condition of severe noise pollution (10% noise in the resonant frequencies). In this case, the inference yields maximum and mean absolute relative errors of 13.95% and 6.36%, respectively. These results demonstrate the robustness and reliability of the presented surrogate model-based BMU for damage identification in the presence of noise in the modal signatures.

Table 1: Surrogate model-based BMU results of the stiffness coefficients θ_i of the 31-bar planar truss structure for different noise levels. Noise level 1: $\eta_1 \sim \mathcal{N}(\mu = 0, \sigma = 1E-2)$ and $\eta_2 \sim \mathcal{N}(\mu = 0, \sigma = 1E-1)$; Noise level 2: $\eta_1 \sim \mathcal{N}(\mu = 0, \sigma = 5E-2)$ and $\eta_2 \sim \mathcal{N}(\mu = 0, \sigma = 5E-1)$; and Noise level 3: $\eta_1 \sim \mathcal{N}(\mu = 0, \sigma = 1E-1)$ and $\eta_2 \sim \mathcal{N}(\mu = 0, \sigma = 1E+0)$.

Bar No.	Parameter	Exact θ_i	Noise Level 1		Noise Level 2		Noise Level 3	
			Mean	Error	Mean	Error	Mean	Error
31	θ_1	0.80	0.76	4.89	0.85	-5.99	0.85	-6.63
1	θ_2	1.00	0.94	6.34	0.93	6.92	0.88	12.44
28	θ_3	0.90	0.90	-0.07	0.90	0.12	0.89	0.90
4	θ_4	0.85	0.90	-5.51	0.91	-6.65	0.91	-6.70
18	θ_5	0.90	0.89	1.05	0.89	1.19	0.90	-0.05
14	θ_6	1.05	0.90	13.81	0.90	13.88	0.90	13.94
7	θ_7	0.90	0.90	-0.21	0.90	0.54	0.91	-1.23
22	θ_8	1.00	0.91	9.24	0.91	8.67	0.91	8.99

5.3. *Case Study III: the Sciri Tower*

This last section reports the application of the proposed approach to a real case study of a historic civic tower located in the city centre of Perugia in Italy (Figure 7 (a)), named *Torre degli Sciri*. The tower is 41 m high with a rectangular cross-section (7.15 x 7.35 m), and it is made of white limestone masonry. Up to the first 17 m, the tower is inserted into a building aggregate with approximate cross-section dimensions of 20 x 25 m. This medieval tower has been the subject of study in several investigations by the authors, and interested readers may refer to references [70, 71] for further information about its architecture.

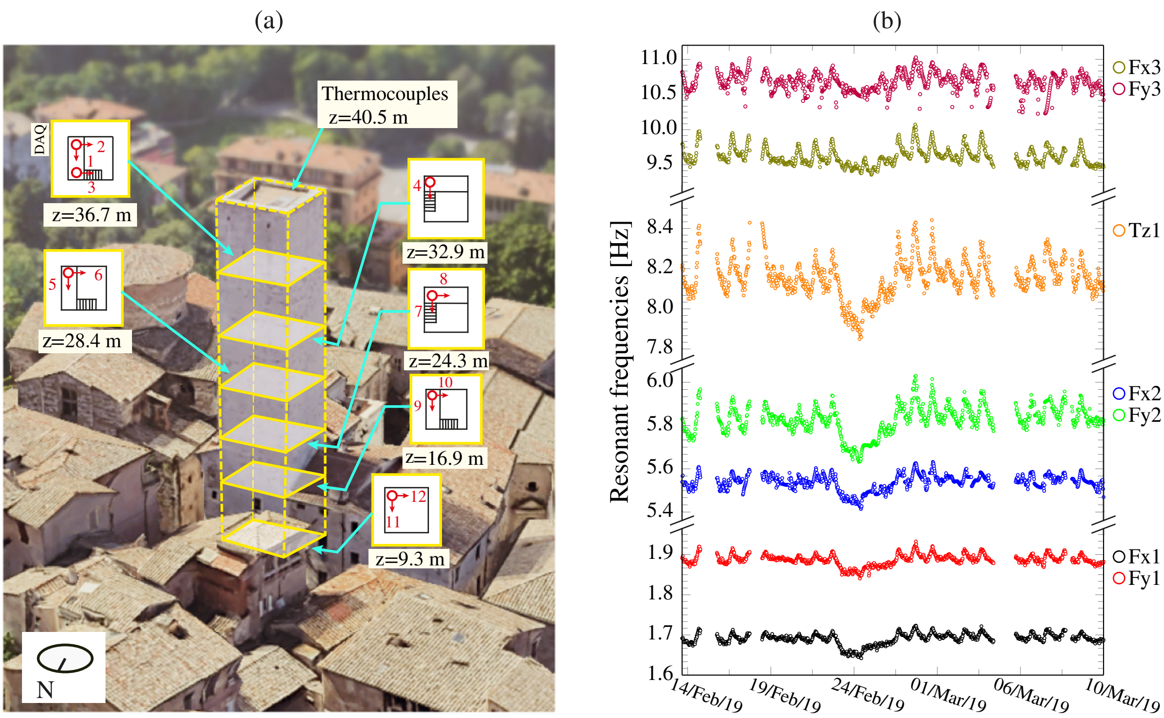

Figure 7: Sensors layout for continuous monitoring of the Sciri Tower (a), and tracking of the modes of vibration since February 13th until March 10th 2019 (b).

A continuous environmental/dynamic monitoring campaign with a relatively large number of sensors was performed from February 13th until March 10th 2019. As shown in Fig. 7 (b), twelve high sensitivity (10 V/g) uniaxial accelerometers model PCB 393B12 were installed at six different heights of the tower, acquiring ambient vibrations at a sampling frequency of 1652 Hz and down-sampled to 40 Hz. Two K-type thermocouples were also installed at the level z = 40.5 m to measure indoor and outdoor temperatures at a sampling frequency of 0.4 Hz. The modal identification of the tower was continuously performed using 30-min long acceleration records via two in-house codes recently developed by the authors and reported in reference [54]. This pair of software codes, named MOVA and MOSS, provide all the necessary tools for the management of long-term integrated SHM systems. In particular, the Covariance-driven Stochastic Subspace Identification (COV-SSI) method was used to identify the modal properties of the Sciri Tower. The parameters used in the identification included maximum and minimum numbers of block rows/columns in the Toeplitz matrix of covariances of 89 (time lag 2.23 s) to 256 (time lag 6.40 s), respectively, with steps of 17, and model's orders running from 20 to 120 with steps of 2. Figure 7 (b) reports the tracking of the modes of vibration of the Sciri Tower. Seven vibration modes have been identified in the frequency range between 0 and 10 Hz as shown in Fig. 8 (a): two flexural modes in NW direction (Fx1 and Fx2), two flexural modes in SW direction (Fy1 and Fy2), one torsional mode, Tz1, and two higher order flexural modes, Fx3, Fy3. Table 2 collects the identified resonant frequencies, damping ratios, and modal phase collinearity (MPC) values exploiting the first 30-min acceleration records acquired in the tower. The MPC values of all the modes are above 95% (classically damped), except for modes Fx2 and Fy2 with values of 84.9% and 80.2%, which indicates that the latter are non-classically damped or the level of excitation is insufficient to correctly identify these mode shapes.

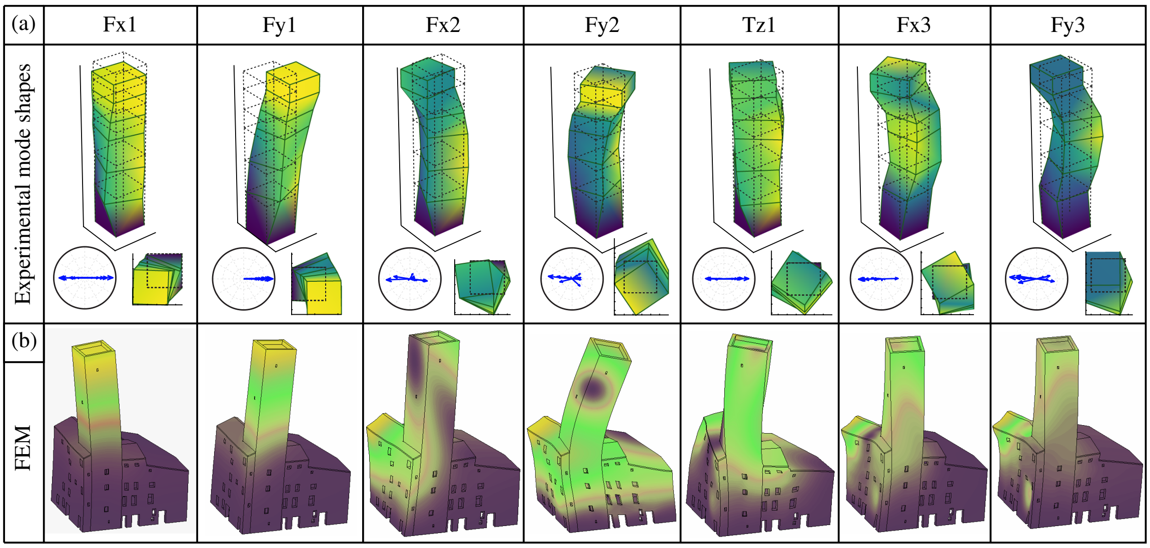

Figure 8: Comparison between experimental (a) and numerical mode shapes (b) of the Sciri Tower.

Table 2: Experimentally identified natural frequencies f_i^{exp}, damping ratios ζ_i and Modal Phase Collinearity (MPC) estimated through COV-SSI on 13th February 2019 at 14:00 UTC.

No	Mode	f_i^{exp} [Hz]	ζ_i [%]	MPC_i [%]	MPD_i [%]
1	Fx1	1.691	0.898	100	0.4
2	Fy1	1.890	0.785	100	0.4
3	Fx2	5.534	2.980	87.0	41.2
4	Fy2	5.826	2.116	72.3	45.6
5	Tz1	8.209	1.777	99.9	4.9
6	Fx3	9.781	1.238	98.7	35.7
7	Fy3	10.814	3.133	93.1	16.4

5.3.1. Parametrization of the FEM of the Sciri Tower

A fully detailed 3D FEM of the building ensemble of the Sciri Tower was built using the commercial software ABAQUS 6.10 in reference [50], and retrieved herein as the basis for the newly proposed BMU approach. The geometry was meshed using ten-node quadratic tetrahedral elements `C3D10` with mean element size of about 50 cm, leading to a total number of elements and nodes of 245148 and 411140, respectively. The material model of the masonry was initially considered as elastic isotropic with Young's modulus E = 4.04 GPa, Poisson's ratio ν = 0.25, and mass density w = 2.20 t/m^3 according to the Italian technical standard for square stone masonry. A two-step model calibration was carried out using first-order sensitivity analysis followed by an inverse calibration using a GA, considering the modal features extracted from the first vibration data acquired on February 13th as reference modal signatures. The resulting comparison between the numerical and experimental modal properties from reference [50] is retrieved herein in Table 3. Good agreements were achieved for modes Fx1, Fy1, Tz1, Fx3 and Fy3 with relative differences in terms of resonant frequencies below 4% and MAC values above 0.84. Conversely, considerably small MAC values were found for modes Fx2 and Fy2, specially the latter one with a value of 0.084. As discussed in our previous work [50], the reason for such a low similarity between the numerical and experimental mode shapes is ascribed to the high complexity of modes Fx2 and Fy2 reported previously in Table 2, which may possibly relate to unmodelled soil-structure interaction effects. For this reason, modes Fx2 and Fy2 are later removed from those used for real-time BMU.

Table 3: Comparison between experimental and numerical modal parameters of the Sciri Tower after the initial calibration by GA.

Mode No.	Resonant frequencies [Hz]			MAC values
	Exp.	Numerical	Rel. Diff. [%]	
Fx1	1.692	1.692	-0.017	0.976
Fy1	1.891	1.886	0.259	0.965
Fx2	5.539	5.591	-0.941	0.757
Fy2	5.830	6.166	-5.760	0.084
Tz1	8.205	7.900	3.720	0.850
Fx3	9.795	9.654	1.445	0.934
Fy3	10.819	10.864	-0.415	0.846

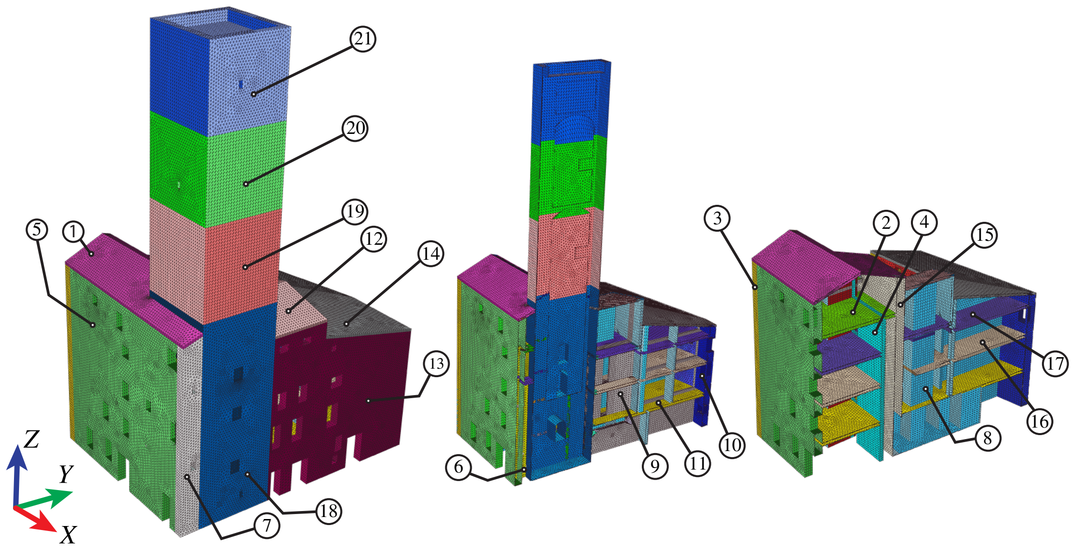

Figure 9: Partitioning of the FEM of the Sciri Tower into 21 macro-elements.

For the subsequent Bayesian inference, the selection of uncertain structural model parameters critically determines the accuracy of the damage identification. A first challenge to be faced regards the circumstance that massive systems such as the Sciri Tower are composed of a large number of structural members, and defects typically develop diffusely across certain parts of the structure. In addition, performing element-wise damage identification is simply infeasible from both a computational and an observability standpoint. To address these limitations, a common approach consists in grouping certain parts of the structure forming macro-elements. The definition of such macro-elements may be conducted leveraging engineering knowledge and more systematic techniques like sensitivity-based clustering. The latter allows one to form in an unsupervised manner a reduced set of clusters (macro-elements) grouping model parameters with similar influence upon the sensitivities of the targeted modal features [23]. In this light, the tower is first densely divided into a large set of 21 sections as sketched in Fig. 9, including ten masonry walls, four floors, three parts of the roof of the building aggregate, and four portions of the tower. The latter is divided into four portions located between heights of 0-18.9 m (18), 18.9-26.8 m (19), 26.8-33.8 m (20), and 33.8-41.0 m (21). Note that the ordering of the partitions in Fig. 9 has been defined according to the clustering results reported hereafter for ease in the discussion. The sensitivities are obtained numerically by individually perturbing the elastic moduli of the 21 sections by ±5%, and the corresponding natural modes are calculated by linear modal analysis of the FEM. Let us note the residual $\mathbf{r} \in \mathbb{R}^{m(N_o+1)}$ as the differences between the perturbed $\widetilde{\mathbf{z}}$ and unperturbed $\mathbf{z}$ modal estimates, i.e. $\mathbf{r} = \widetilde{\mathbf{z}} - \mathbf{z}$, and $\Delta\theta_i$ the corresponding perturbation of the i-th model parameter. Then, the ij-th component of the sensitivity matrix $\mathbf{S} \in \mathbb{R}^{m(N_o+1)\times M}$ can be obtained by finite differences as:

$$S_{ij} = \frac{r_j}{\Delta\theta_i}. \tag{50}$$

In this particular case study, $m = 7$ natural modes are considered with $N_o = 12$ measured DOFs, leading to a sensitivity matrix of dimension 21×91. Then, a distance function is required to compute the proximity between sensitivities. The cosine distance is used in this work to evaluate the dissimilarity between pairs of sensitivities $(\boldsymbol{\alpha}, \boldsymbol{\beta})$ as:

$$\text{cosine distance}\,(\boldsymbol{\alpha}, \boldsymbol{\beta}) = 1 - \frac{\boldsymbol{\alpha}^{\mathrm{T}}\boldsymbol{\beta}}{\boldsymbol{\alpha}^{\mathrm{T}}\boldsymbol{\alpha}\boldsymbol{\beta}^{\mathrm{T}}\boldsymbol{\beta}}. \tag{51}$$

Note that the cosine distance as defined in Eq. (51) is susceptible to become a skewed metric when combining both frequency and mode shape sensitivities. Indeed, there is no natural scale for mode shapes, which can be arbitrarily normalized. It is thus necessary to scale the residual sensitivity vectors to accommodate both quantities. Inspired by the work by Bartilson *et al.* [72] who proposed an objective-consistent scaling of cosine distances, scaled sensitivities $\overline{S}_{ij}$ are considered in this work as:

$$\overline{S}_j = \begin{bmatrix} \mathbf{W}_f & \mathbf{0} \\ \mathbf{0} & \mathbf{W}_\varphi \end{bmatrix} \begin{bmatrix} r_f/\Delta\theta_j \\ r_\varphi/\Delta\theta_j \end{bmatrix}, \tag{52}$$

where r_f and r_φ concentrate the residuals in terms of resonant frequencies and mode shapes, respectively, and $\mathbf{W}_f$ and $\mathbf{W}_\varphi$ are residual weighting matrices reflecting the relative contribution of resonant frequencies and mode shapes to the sensitivities. As reported in reference [72], $\mathbf{W}_f$ and $\mathbf{W}_\varphi$ can be estimated as the inverse of the measurement covariance matrices of resonant frequencies and mode shapes, respectively. In this work, given that sensors are only located in the Sciri Tower and the modal displacements are not monitored in the building aggregate, the weighting matrices are defined in a simplified manner as $\mathbf{W}_f = \alpha\mathbf{I}$ and $\mathbf{W}_\varphi = \beta\mathbf{I}$. Weighting parameters α and β concentrate the relevance of the contribution of resonant frequencies and mode shapes to the sensitivity matrix, respectively. On this basis, a hierarchical clustering approach has been applied to cluster the initial 21 model parameters into a reduced number of macro-elements with similar sensitivities. To do so, the Unweighed Pair Group Method with Arithmetic Mean (UPGMA) [73] has been implemented as the linkage method. With the aim of keeping at least three macro-elements between partitions 18 to 21 in Fig. 9 to discretize the tower, a β/α ratio of 12 was found suitable after some manual tuning. In this light, the hierarchical binary tree associated with the sensitivities of the partitions of the Sciri Tower is shown in Fig. 10 (a). The tree has been cut at a distance of 0.39, forming 9 clusters labelled with C1 to C9. The corresponding macro-elements are depicted in Fig. 10 (b). Note that the resulting discretization of the tower only includes three macro-elements, merging the previously defined top two elements (20,21) in Fig. 9 into C9. The resulting sensitivities grouped by macro-elements C1 to C9 are presented as 3-D bar plots in Figs. 11 (a) and (b) in terms of resonant frequencies and mode shapes, respectively. The cosine distance calculation utilized the complete set of mode shape sensitivities (5 modes with 12 DOFs per mode), but the results in Fig. 11 (b) are represented by MAC sensitivities for clarity.

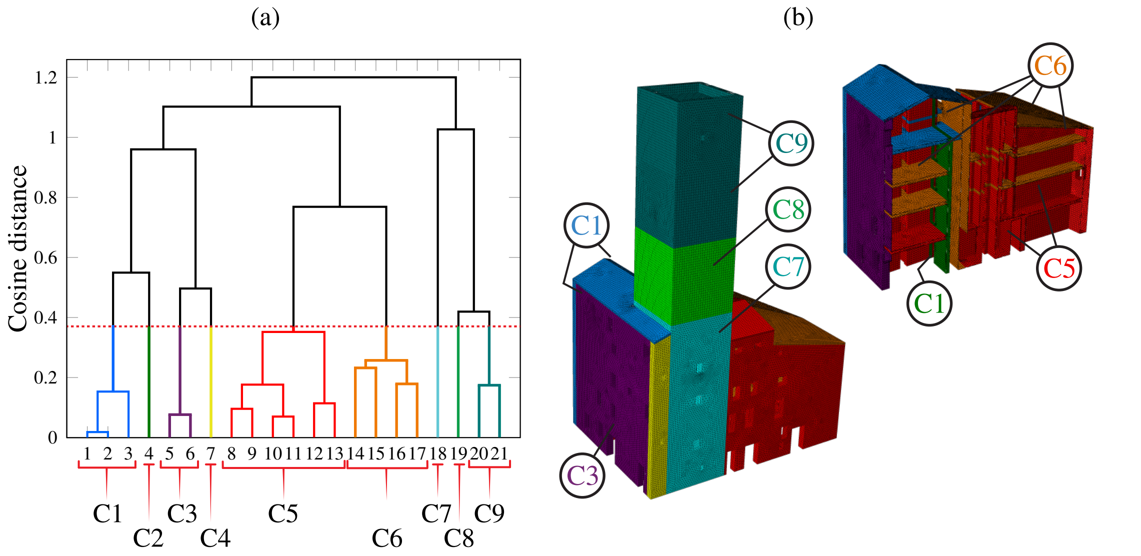

Figure 10: Hierarchical binary tree of sensitivities to the Young's moduli of the 21 sections of the Sciri Tower (a) and resulting macro-element clusters (b).

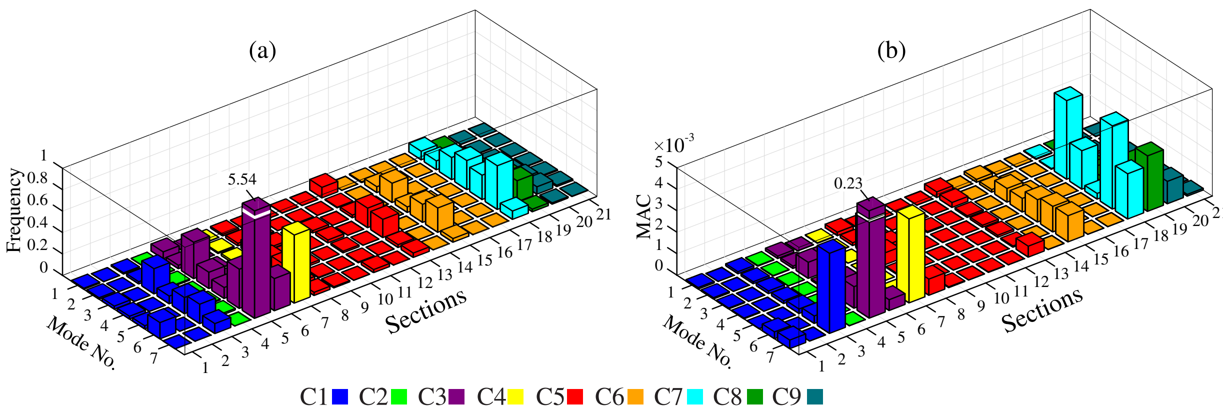

Figure 11: Frequency (a) and mode shape sensitivities (b) of the 21 sections of the Sciri Tower organized into 9 macro-elements.

5.3.2. Training of the surrogate model and initial FEM updating

According to the previous parametrization, the model updating parameters θ_i, $i = 1, \ldots, 9$, to be identified in the subsequent Bayesian inference are defined as linear proportionality coefficients of the elastic moduli E_i of the corresponding macro-elements, i.e. $E_i = \theta_i \cdot E_{i,0}$, with $E_{i,0}$ being the nominal (undamaged) value of the Young's modulus of the i-th macro-element. It is important to mention that every linear modal analysis of the 3D FEM takes around 5 minutes on a 4-core Intel Xeon CPU 3.30 GHz (64 GB RAM) computer. Given the large number of forward model evaluations involved in BMU, the direct use of the FEM is infeasible so it becomes imperative to build a more computationally efficient surrogate model. To this aim, the PC-Kriging surrogate model previously introduced in Section 3 is adopted herein. For the construction of the surrogate models, the design variables θ_i are assumed to be uniformly distributed in a considerably large interval [0.7, 1.3]. The first seven resonant frequencies and mode shapes of the Sciri Tower are taken into account, which amounts to a total of 91 uni-dimensional meta-models. To determine the optimal dimension of the design space, a convergence analysis is firstly conducted considering different design spaces sampled by LHS with increasing sizes of N = 50, 100, 200, 500, 1000, 2000, and 3000 samples. Figure 12 (a) shows the convergence curves of the average values of the resonant frequencies of the FEM of the Sciri Tower versus the size of the design space. The error bars in this figure represent the variance of the distributions. In view of these results, a design space of N = 500 samples achieves convergence so it is chosen to train the meta-model. The histograms of the resonant frequencies of the tower obtained by the selected training set are shown in Fig. 12 (b).

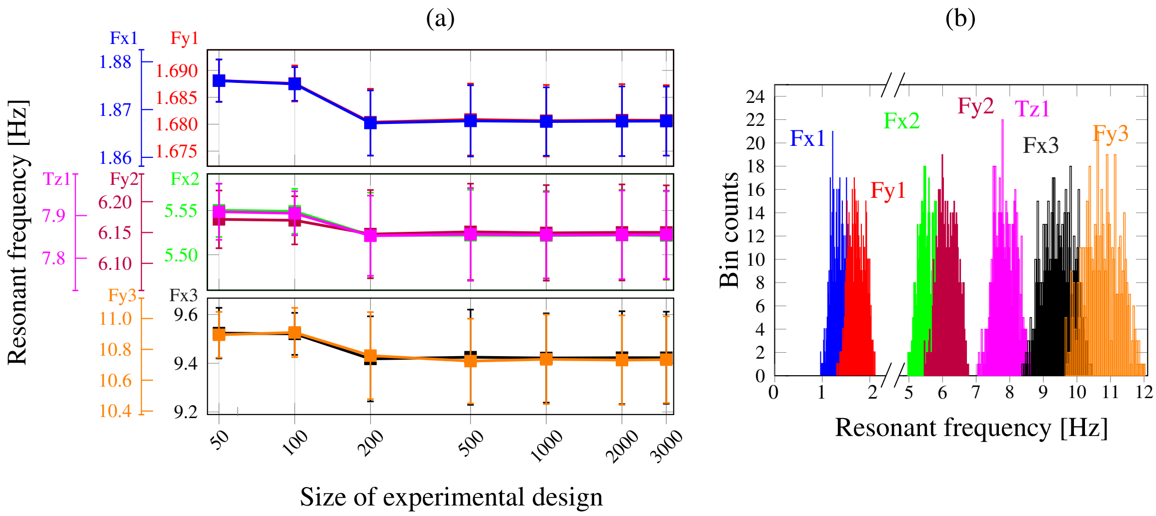

Figure 12: Convergence analysis of the mean values of the natural frequencies obtained by linear modal analysis of the FEM of the Sciri Tower versus the size of the design space (a), and histograms of the resonant frequencies obtained for a design space of N = 500 samples (b). The error bars in (a) denote the variance of the distributions.

Legendre polynomials of orders ranging from 2 to 6 are selected to build the PCE basis with a q-norm of 0.6, and the leave-one-out error is used to select the optimal expansions. To evaluate the accuracy of the constructed surrogate model, the largest design space of 3000 samples is used as the validation set. The resulting scatter plots of the resonant frequencies obtained by the FEM and the predictions by the surrogate model are shown in Fig. 13. The low scatter of the points around the diagonal line ($R^2 \approx 1$) and maximum root-mean-square errors (RMSEs) of 5E-2 corroborate that the surrogate models are formed with accuracy. In addition, very close fittings of the mode shapes have been also obtained, with maximum J_{MAC} metric values of the order of E-3. Note that the computational time required to evaluate the surrogate model only takes about 0.5 ms, which ensures its applicability in the upcoming continuous BMU. Let us also indicate that the PCE-Kriging meta-model outperforms standard PCE in this case study, whose RMEs almost double the values reported in Fig. 13.

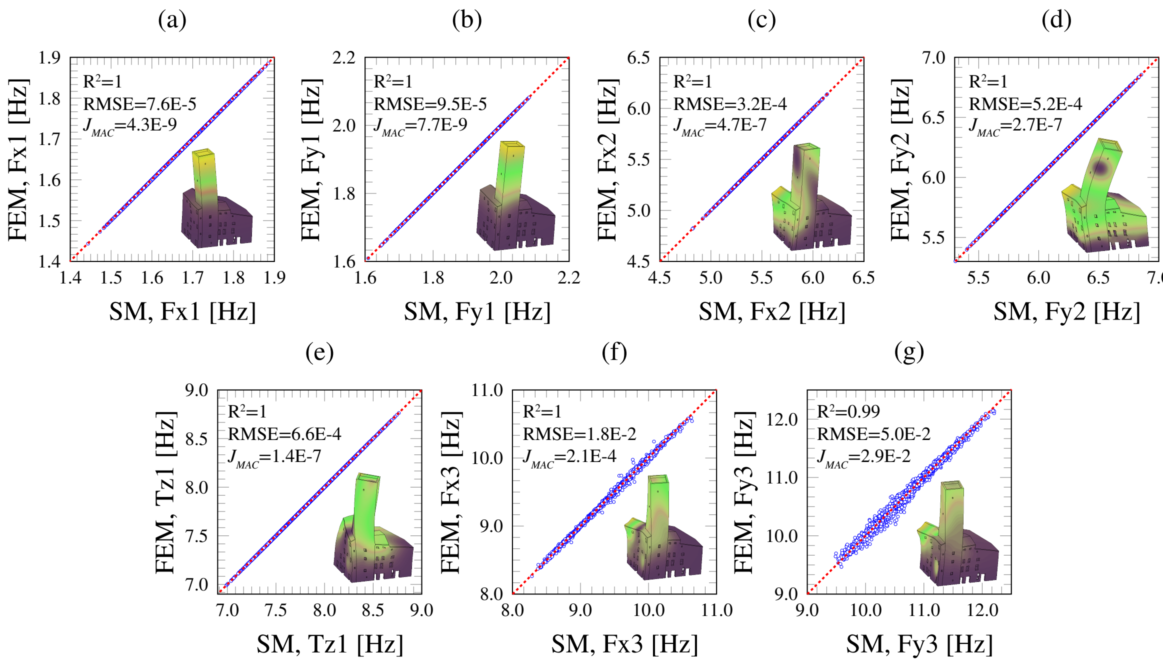

Figure 13: Scatter plot of the PCE-Kriging meta-model (500 training samples) with respect to the FEM of the Sciri Tower for the first seven natural modes (validation set of 3000 samples, RMSE = Root Mean Squared Error).

Once the meta-model is constructed, the experimental modal features reported above are used to conduct continuous BMU. Note that the resonant frequencies previously shown in Fig. 7 exhibit strong variations induced by changes in the environmental conditions (both daily and seasonal to a certain extent). In order to filter out such variations, a data normalization approach combining Multiple Linear Regression (MLR) and Principal Component Analysis (PCA) has been implemented (refer to reference [11] for further details on the theoretical formulation). Firstly, the modal signatures until May 3rd (800 samples) are selected as the training period to build the data normalisation model. The time series of environmental temperature recorded by the two thermocouples located at the top of the tower (see Fig. 14 (a)) measuring indoor and outdoor of the tower are used as predictors in the MLR model. Then, the residual variances in the resonant frequencies due to unmodelled operational factors are further minimized using PCA. To do so, the residuals between the resonant frequencies and the predictions of the MLR model are decomposed using PCA and one principal component (explaining more than 90% of the total variance) is kept to reconstruct the residuals. Figure 14 (b) shows the comparison between the time series of experimental frequencies and the predictions of the MLR/PCA model. Once constructed using the training period dataset, the MLR/PCA model is applied to normalize the remaining resonant frequencies in the damage assessment period until March 10th. On this basis, the time series of normalised resonant frequencies to be included in the Bayesian inference are obtained as their average values in the training period plus the residuals computed between the predictions of the MLR/PCA model and the experimental data all throughout the monitoring period. On the other hand, the mode shapes are barely affected by the environmental conditions and, therefore, no data normalisation has been conducted. Following the previous discussion on the dynamic identification results reported in Table 2, mode shapes Fx2 and Fy2 are excluded in the subsequent St-Id.

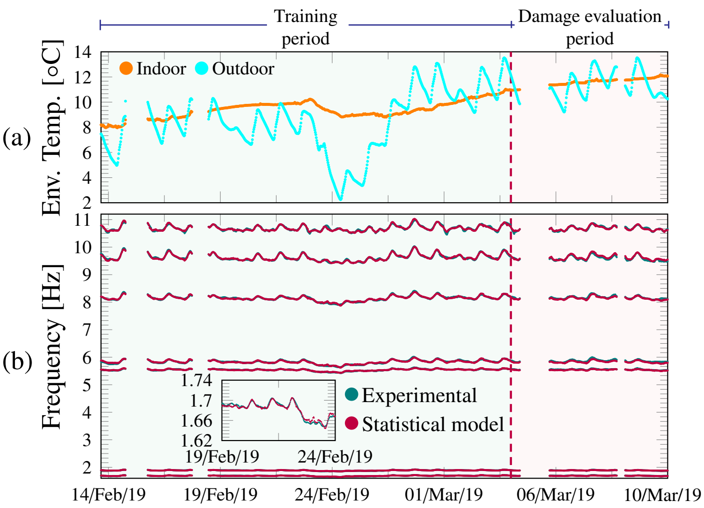

Figure 14: Time series of environmental temperature (a) and comparison between the experimental resonant frequencies of the Sciri Tower and the predictions by the MLR/PCA model (b).

An initial surrogate-model based BMU is carried out considering the whole normalized training period as reported in Fig. 15. Since mode shape displacements were only obtained in the tower and no information was acquired in the building aggregate, the inference limited to the identification of parameters θ_9, θ_8 and θ_7, corresponding to the macro-elements pertaining to the tower. Moreover, given the relatively low number of measured modal displacements, the likelihood function formulated in terms of MAC values in Eq. (36) has been implemented herein. Gaussian prior distributions with a mean value of 1 and a standard deviation of 0.1 are defined for all the fitting parameters. During the analyses, a total number of 3000 samples with a burning time of 900 samples are drawn by the previously introduced Bayesian inference approach. The Gaussian proposal is initially defined as a diagonal covariance matrix of value 1E-2 and scaled by the factor $s_d = 2.4^2/d$. In the DR step, the covariance matrix of the proposal distribution is scaled down by a factor $\gamma = 0.1$. The initial location state θ_0 is defined by considering all the uncertain parameters equal to 1.0, and the initial prediction errors have been estimated from the statistical analysis of the time series of identified modal signatures as $\sigma_f^2 = 3.0\%$ and $\sigma_\varphi^2 = 0.9\%$ (Eq. (36)). All things considered, the selected hyperparameters led to an average acceptance rate of 67%. Figure 15 (a) presents a three-dimensional scatter plot of the Markov chain on a colour scale representing the normal kernel smoothed probability values of the samples ($\hat{p}\,(\mathbf{x}|\,\mathbf{d}\,)$, normalized between 0 and 1). The statistical analysis of the marginal chains is reported in Fig. 15 (b). It is clearly noted that, in accordance with the sensitivity analysis previously reported in Fig. 11, the dispersion of the PDFs of the fitting parameters increases in height. Lastly, it is important to highlight that the total computational time to obtain the Markov chains amounts to about 20 min, which enables the integration of the proposed approach into a continuous SHM scheme, given that OMA is carried out every 30 minutes of data recording.

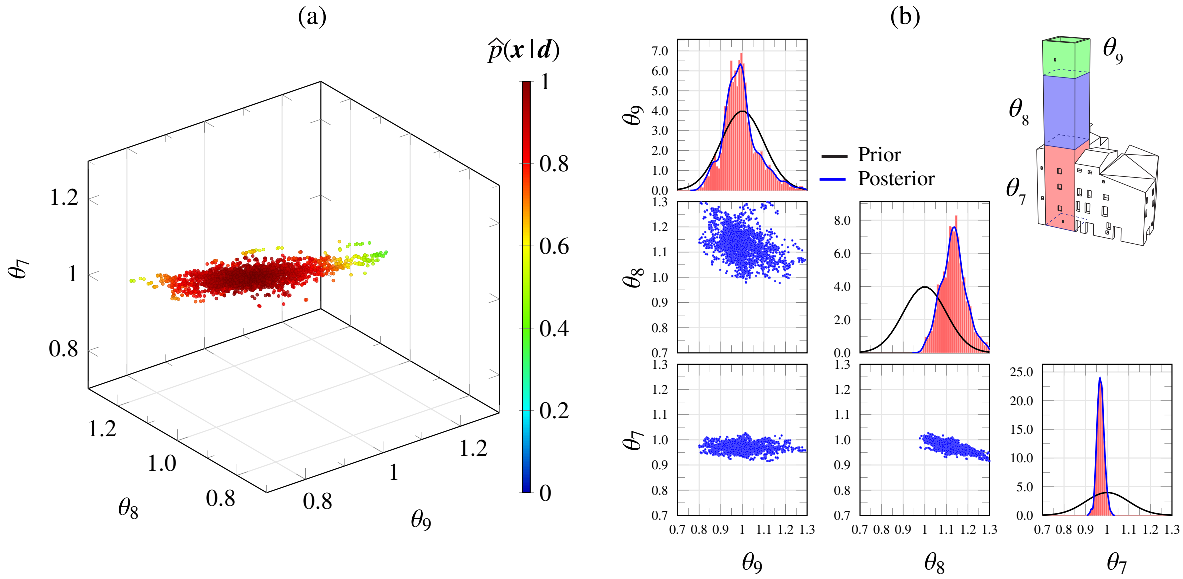

Figure 15: Bayesian identification results of the stiffness coefficients θ_9, θ_8 and θ_7 of the Sciri Tower considering the modal signatures during the training period (800 samples, from February 13^{th} to May 3^{rd}, 2019). Three-dimensional scatter plot of the obtained Markov chain (a), and correlation analysis (b).

5.3.3. *Continuous FEM updating - Damage Identification*

In order to assess the effectiveness of the proposed damage identification approach, four different synthetic damage scenarios have been created on the basis of the 3D FEM of the Sciri Tower as shown in Fig. 16. The scenarios have been defined by eliminating the stiffness of certain parts of the FEM to simulate crack-like defects. In particular, Damage Scenarios 1, 2, and 4 include damage in the macro-elements C9, C8 and C7, respectively, while Damage Scenario 3 simulates the detachment between the east façade of the tower and the building aggregate. The corresponding modal signatures have been obtained by linear modal analysis of the 3D FEM, and the resulting damage-induced frequency decays with respect to the undamaged condition are reported in Table 4. Note that, according to previous experience, anomalies in the time series of resonant frequencies are identifiable by standard novelty analysis techniques when relative damage-induced frequency decays approximately exceed 1%. Therefore, according to the decays reported in Table 4, Damage Scenario 1 can be considered as a mild damage condition, Damage Scenarios 2 and 3 as moderate damage conditions, and Damage Scenario 4 as a severe damage condition. These frequency decays have been incorporated in the time series of resonant frequencies in the shape of constant mean shifts. On the other hand, the mode shapes corresponding to the damage conditions are directly used in the damage assessment period. Note that the parametrization defined in Section 5.3.1 does not account for model parameters strictly related to the affected elements in the damage scenarios in Fig. 16. Instead, the selected parametrization was designed to offer a general model to identify structural defects conceivable as global stiffness reductions in horizontal sections of the tower. Therefore, an important aspect in subsequent assessment of the damage identification capabilities of the proposed approach regards its robustness to structural defects not exactly reproduced in the model parametrization.

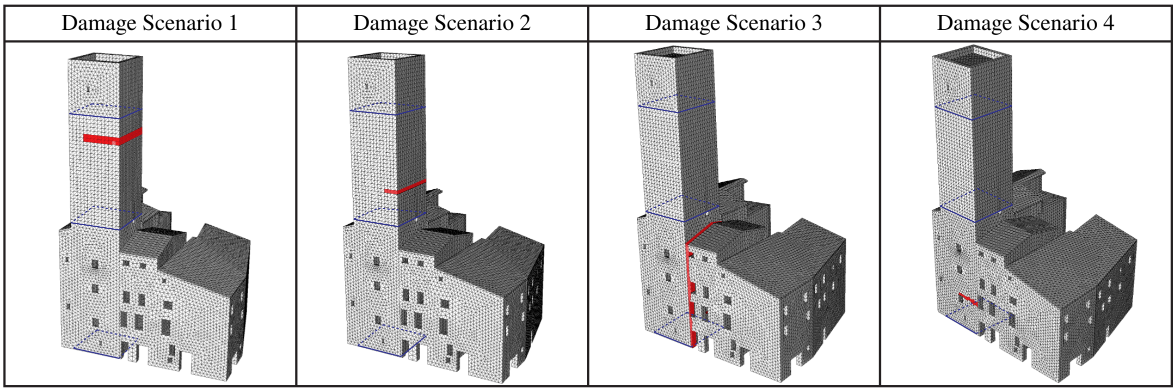

Figure 16: Synthetic damage scenarios defined using the 3D FEM of the Sciri Tower.

Table 4: Damage-induced decays in the resonant frequencies of the Sciri Tower under Damage Scenarios 1 to 4.

	Frequency decays [%]						
Case scenario	Mode 1	Mode 2	Mode 3	Mode 4	Mode 5	Mode 6	Mode 7
Damage Scenario 1	-0.01	-0.02	-0.05	-0.05	-0.02	-0.12	-0.02
Damage Scenario 2	-0.49	-0.58	-1.00	-1.51	-1.55	-3.29	-0.35
Damage Scenario 3	-1.62	-1.70	-1.20	-2.69	-2.70	-3.81	-0.27
Damage Scenario 4	-6.24	-3.36	-1.95	-1.12	-9.11	-1.30	-0.85

To alleviate the computational burden, the modal data have been split into datasets containing 48 hours of measurements with 24 hours overlap, which amounts to a total of 20 model identifications. Nevertheless, as already mentioned the computational time involved in the MCMC sampling amounts to about 20 minutes, being possible to reduce the time resolution in the St-Id if needed. The covariance matrix of the proposal distribution has been taken as the covariance matrix of the Markov chains obtained by the previous BMU in Section 5.3.1 exploiting the training period, as well as the initial prediction errors, while the rest of the identification parameters have been kept constant. The obtained marginal PDFs for the four damage scenarios are furnished in Fig. 17. It is observed that no clear variations can be found for Damage Scenario 1, while reasonably good identification results were obtained for the rest of the damage scenarios. The damage identification limitations in Section C9 are attributable to the low sensitivity of the modal signatures of the tower to variations in the stiffness of the upper part of the tower as previously shown in Fig. 11. In order to provide a comprehensive metric for damage identification, a damage index D_i is presented in Fig. 18 as the relative percent differences of the medians of the Markov chains with respect to the initial one obtained in the training period. The results in this figure confirm the previous discussion, being possible to clearly identify damage in Scenarios 2 to 4. Damage Scenario 2 is characterized by marked stiffness reductions in macro-elements C8 and C9 (see Fig. 17 (b)). Although this damage condition does not explicitly affect the stiffness of C9, the reductions in this macro-element are ascribed to ill-conditioning limitations given the low modal sensitivity related to the stiffness of the top section of the tower. This circumstance may be also explained by the inherent limitations of the adopted parametrization, since no model parameter accounting for the local stiffness reduction in the elements affected by the crack in Damage Scenario 2 are considered. This aspect may facilitate the obtained solution affecting C8 and C9 to appear more likely from a Bayesian perspective than the solution only affecting C8 (where the crack is truly located).

Finally, it is noted that damage-induced variations in Damage Scenario 3 concentrate in macro-element C8 (θ_8) with some decreases in C7 (θ_7). This indicates that given the defined parametrization, the implemented BMU approach finds as the most probable solution for the given observations the one with concentrated stiffness reductions in the middle section and with only moderate decreases in the bottom part of the tower. Despite Section C8 is directly in contact with the building aggregate, note that the detachment of the tower from the building aggregate in Damage Scenario 3 cannot be easily modelled by affecting the stiffness of the defined macro-elements. This circumstance evidences a natural limitation of any model parametrization that does not explicitly represent a certain damage mechanism, as it is in this case since there is no particular parameter accounting for the connection with the building aggregate. In fact, observe that Damage Scenario 4, which effectively affects the stiffness of C7, does concentrate reductions in the PDF of θ_8. In this case, some spurious increases in the stiffness of C8 are found, which are ascribed to observability limitations related to the defined parametrization. Despite all the challenges that unavoidably exist when monitoring complex masonry structure like the investigated one, these results demonstrate the potentials of the presented surrogate model-based BMU for online damage identification of large-scale structures.

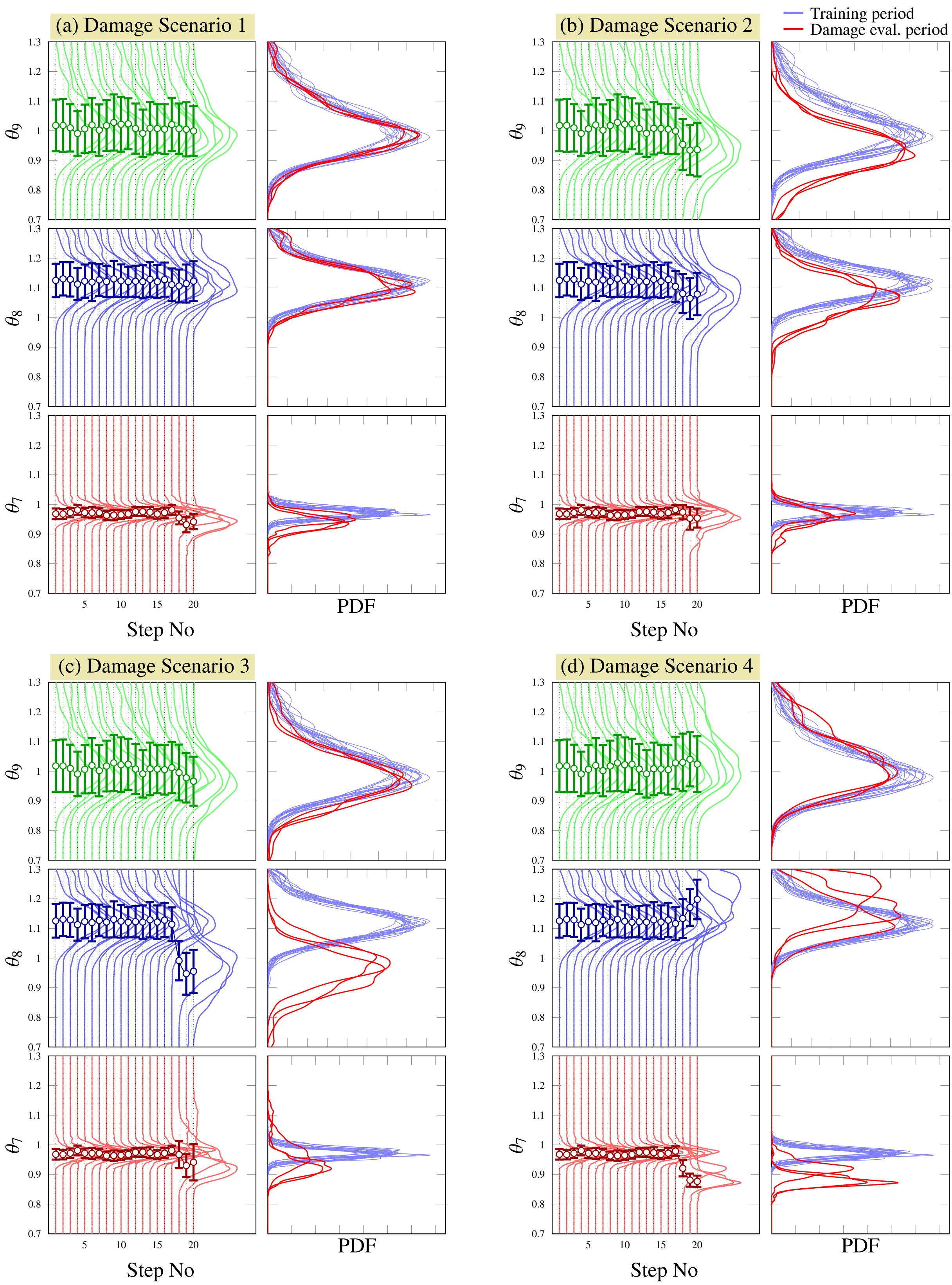

Figure 17: Bayesian damage identification results of the Sciri Tower throughout all the monitoring period from February 13th until March 10th 2019 considering four synthetic damage scenarios (a to d). Error bars indicate standard deviation values.

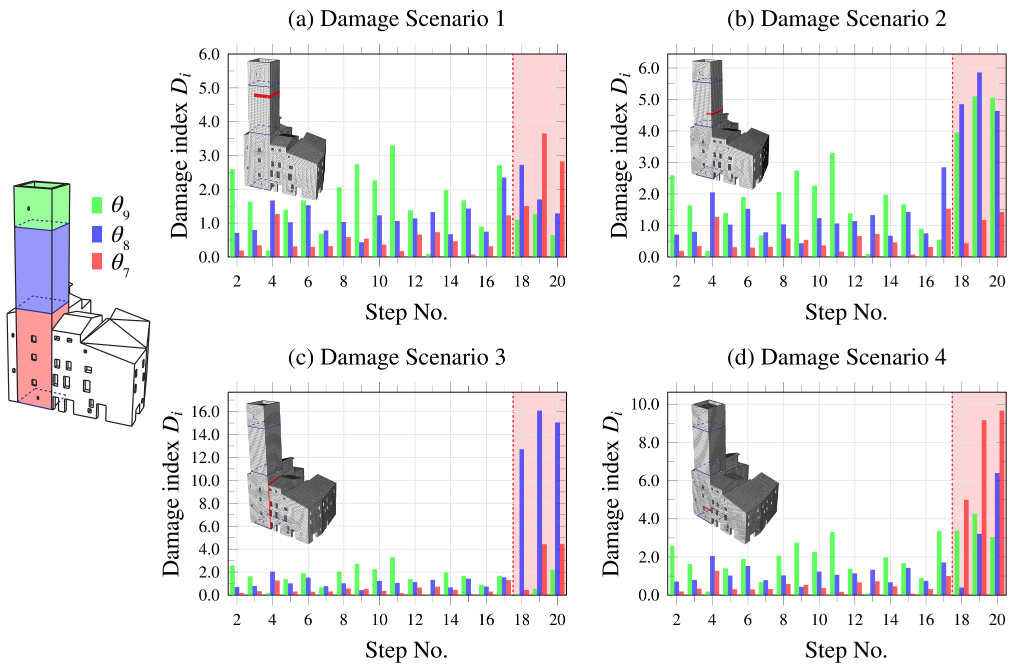

Figure 18: Damage indices D_i obtained as the relative percent differences of the medians of the Markov chains of parameters θ_9, θ_8 and θ_7 of the Sciri Tower with respect to the initial chain obtained in the training period for Damage Scenarios 1 to 4 (a to d).

6. Conclusions

This work has presented a high-fidelity surrogate modelling approach combining sparse adaptive PCE and Kriging meta-modelling for MCMC BMU of large-scale structures, with a focus on its implementation in real-time SHM of large-scale structures. The LAR algorithm has been adopted to automatically define the optimal order of the PCE and only retain the most significant terms in the expansion, minimizing the computational burden of the training and evaluation of the meta-model. The optimized PCE then plays the role of the trend term in a Kriging predictor, while the stochastic term is fitted through global optimization. Once built, the surrogate model is inserted into a DRAM MCMC approach to perform BMU exploiting monitoring data from long-term vibration-based SHM systems. The implemented MCMC approach combines AM sampling and DR, so attaining both global and local adaptation capabilities. This combination results in an MCMC algorithm that constantly alternates between larger and smaller steps in the Markov chain, allowing for better exploration of the parameters space and sample from multimodal PDFs. The effectiveness of the proposed methodology has been demonstrated through three case studies: (i) an analytical benchmark; (ii) a planar truss structure; and (iii) a real case study of a complex historical tower, the Sciri Tower in Italy. The accuracy and robustness of the developed meta-model have been validated by the first two benchmark cases, while the last case study has evidenced the real-time capabilities of the surrogate mode-based BMU when exploiting long-term SHM data. In particular, the time series of modal signatures extracted by automated OMA during three weeks have been utilized to conduct continuous St-Id of a high-fidelity 3D FEM of the Sciri Tower. Finally, four different synthetic damage scenarios have been generated to evidence the potentials of the proposed approach for damage detection, localization and quantification. Overall, the presented results have demonstrated that the proposed BMU approach is compatible with real-time SHM owing to the computational efficiency of the meta-model and the MCMC sampling, enabling its incorporation into continuous damage identification applications for the autonomous management of civil infrastructures. Although the computational efficiency of the DRAM algorithm sufficed for the purpose of the present work, future developments may involve the implementation of advanced sampling techniques such as parallelized TMCMC, BBL or nested sampling techniques with superior capabilities to handle engineering problems with large numbers of model parameters.

Future developments involve the implementation of pathology-specific model parametrizations to minimise misclassifications of damage patterns. The definition of multiple model parametrizations (e.g. simulating the appearance of earthquake-induced X-cracks, or vertical cracks due to differential settlements) would firstly allow to establish safety-related thresholds in terms of frequency decays and variations of the modal displacements. Secondly, the implementation of model selection techniques would allow to infer the most likely damage mechanism being activated after a structural anomaly is detected, thus minimizing localization errors due to parametrization limitations.

Acknowledgements

This work was supported by the Italian Ministry of Education, University and Research (MIUR) through the funded project of national interest "DETECT-AGING - Degradation Effects on sTructural safEty of Cultural heriTAGe constructions through simulation and health monitorING" (Protocol No. 201747Y73L).

References

[1] G. M. Calvi, M. Moratti, G. J. O'Reilly, N. Scattarreggia, R. Monteiro, D. Malomo, P. M. Calvi, R. Pinho, Once upon a time in Italy: The tale of the Morandi Bridge, Structural Engineering International 29 (2) (2019) 198–217.

[2] G. Nyikos, N. Ermasova, Public Capital Infrastructure Management: Cases of Germany, Hungary and the USA, International Journal of Public Administration (2021) 1–25.

[3] ASCE, 2021 Report Card for America's Infrastructure, Tech. rep. (2021).

[4] European Commission, Discussion paper–'State of infrastructure maintenance'. (Mar. 2019).

[5] Ministero delle Infrastrutture e dei Trasporti Consiglio Superiore dei Lavori Pubblici, Linee guida per la classificazione e gestione del rischio, la valutazione della sicurezza ed il monitoraggio dei ponti esistenti (2020).

[6] H. P. Chen, Structural health monitoring of large civil engineering structures, John Wiley & Sons, 2018.

[7] M. Mishra, P. B. Lourenço, G. V. Ramana, Structural health monitoring of civil engineering structures by using the internet of things: A review, Journal of Building Engineering (2022) 103954.

[8] S. Beskhyroun, N. Navabian, L. Wotherspoon, Q. Ma, Dynamic behaviour of a 13-story reinforced concrete building under ambient vibration, forced vibration, and earthquake excitation, Journal of Building Engineering 28 (2020) 101066.

[9] G. Zini, M. Betti, G. Bartoli, A quality-based automated procedure for operational modal analysis, Mechanical Systems and Signal Processing 164 (2022) 108173.

[10] V. Nicoletti, D. Arezzo, S. Carbonari, F. Gara, Dynamic monitoring of buildings as a diagnostic tool during construction phases, Journal of Building Engineering 46 (2022) 103764.

[11] E. García-Macías, F. Ubertini, Integrated SHM Systems: Damage Detection Through Unsupervised Learning and Data Fusion, Springer, 2022.

[12] V. Giglioni, E. García-Macías, I. Venanzi, L. Ierimonti, F. Ubertini, The use of receiver operating characteristic curves and precision-versus-recall curves as performance metrics in unsupervised structural damage classification under changing environment, Engineering Structures 246 (2021) 113029.

[13] A. Meixedo, J. Santos, D. Ribeiro, R. Calçada, M. D. Todd, Online unsupervised detection of structural changes using train-induced dynamic responses, Mechanical Systems and Signal Processing 165 (2022) 108268.

[14] P. Cawley, Structural health monitoring: Closing the gap between research and industrial deployment, Structural Health Monitoring 17 (5) (2018) 1225–1244.

[15] V. Arora, Comparative study of finite element model updating methods, Journal of Vibration and Control 17 (13) (2011) 2023–2039.

[16] M. I. Friswell, J. E. Mottershead, H. Ahmadian, Finite-element model updating using experimental test data: parametrization and regularization, Philosophical Transactions of the Royal Society of London. Series A: Mathematical, Physical and Engineering Sciences 359 (1778) (2001) 169–186.

[17] T. Marwala, Finite-element-model updating using computional intelligence techniques: Applications to structural dynamics, Springer, 2010.

[18] N. F. Alkayem, M. Cao, Y. Zhang, M. Bayat, Z. Su, Structural damage detection using finite element model updating with evolutionary algorithms: a survey, Neural Computing and Applications 30 (2) (2018) 389–411.

[19] R. Hou, Y. Xia, Review on the new development of vibration-based damage identification for civil engineering structures: 2010-2019, Journal of Sound and Vibration 491 (2021) 115741.

[20] B. Titurus, M. I. Friswell, Regularization in model updating, International Journal for numerical methods in engineering 75 (4) (2008) 440–478.

[21] H. Ahmadian, G. M. L. Gladwell, F. Ismail, Parameter selection strategies in finite element model updating, Journal of Vibration and Acoustics 119 (1) (1997) 37–45.

[22] H. P. Wan, W. X. Ren, Parameter selection in finite-element-model updating by global sensitivity analysis using Gaussian process metamodel, Journal of Structural Engineering 141 (6) (2015) 04014164.

[23] D. T. Bartilson, J. Jang, A. W. Smyth, Finite element model updating using objective-consistent sensitivity-based parameter clustering and Bayesian regularization, Mechanical Systems and Signal Processing 114 (2019) 328–345.

[24] X. W. Zheng, H. N. Li, H. L. Lv, L. S. Huo, Y. Y. Zhang, Bayesian-based seismic resilience assessment for high-rise buildings with the uncertainty in various variables, Journal of Building Engineering (2022) 104321.

[25] K. V. Yuen, Bayesian methods for structural dynamics and civil engineering, John Wiley & Sons, 2010.

[26] Y. Huang, C. Shao, B. Wu, J. L. Beck, H. Li, State-of-the-art review on Bayesian inference in structural system identification and damage assessment, Advances in Structural Engineering 22 (6) (2019) 1329–1351.

[27] H. F. Lam, J. H. Yang, S. K. Au, Markov chain Monte Carlo-based Bayesian method for structural model updating and damage detection, Structural Control and Health Monitoring 25 (4) (2018) e2140.

[28] S. H. Cheung, S. Bansal, A new Gibbs sampling based algorithm for Bayesian model updating with incomplete complex modal data, Mechanical Systems and Signal Processing 92 (2017) 156–172.

[29] A. Lye, A. Cicirello, E. Patelli, Sampling methods for solving Bayesian model updating problems: A tutorial, Mechanical Systems and Signal Processing 159 (2021) 107760.

[30] R. Rocchetta, M. Broggi, Q. Huchet, E. Patelli, On-line Bayesian model updating for structural health monitoring, Mechanical Systems and Signal Processing 103 (2018) 174–195.

[31] D. Straub, I. Papaioannou, Bayesian updating with structural reliability methods, Journal of Engineering Mechanics 141 (3) (2015) 04014134.

[32] L. Xu, M. Hu, C. Fan, Probabilistic electrical load forecasting for buildings using Bayesian deep neural networks, Journal of Building Engineering 46 (2022) 103853.

[33] J. Luo, M. Huang, C. Xiang, Y. Lei, Bayesian damage identification based on autoregressive model and MH-PSO hybrid MCMC sampling method, Journal of Civil Structural Health Monitoring 12 (2) (2022) 361–390.

[34] J. Li, Y. Huang, P. Asadollahi, Sparse Bayesian learning with model reduction for probabilistic structural damage detection with limited measurements, Engineering Structures 247 (2021) 113183.

[35] H. Sun, A. Mordret, G. A. Prieto, M. N. Toksöz, O. Büyüköztürk, Bayesian characterization of buildings using seismic interferometry on ambient vibrations, Mechanical Systems and Signal Processing 85 (2017) 468–486.

[36] I. Behmanesh, B. Moaveni, Accounting for environmental variability, modeling errors, and parameter estimation uncertainties in structural identification, Journal of Sound and Vibration 374 (2016) 92–110.

[37] G. Bartoli, M. Betti, A. M. Marra, S. Monchetti, A Bayesian model updating framework for robust seismic fragility analysis of non-isolated historic masonry towers, Philosophical Transactions of the Royal Society A 377 (2155) (2019) 20190024.

[38] X. Zhou, C.-W. Kim, F.-L. Zhang, K. C. Chang, Vibration-based Bayesian model updating of an actual steel truss bridge subjected to incremental damage, Engineering Structures 260 (2022) 114226.

[39] W. Zhao, F. Fan, W. Wang, Non-linear partial least squares response surface method for structural reliability analysis, Reliability Engineering & System Safety 161 (2017) 69–77.

[40] G. Blatman, B. Sudret, An adaptive algorithm to build up sparse polynomial chaos expansions for stochastic finite element analysis, Probabilistic Engineering Mechanics 25 (2) (2010) 183–197.

[41] J. M. Bourinet, Rare-event probability estimation with adaptive support vector regression surrogates, Reliability Engineering & System Safety 150 (2016) 210–221.

[42] Z. Wang, A. Shafieezadeh, Highly efficient Bayesian updating using metamodels: An adaptive Kriging-based approach, Structural Safety 84 (2020) 101915.

[43] P. Ni, J. Li, H. Hao, Q. Han, X. Du, Probabilistic model updating via variational Bayesian inference and adaptive Gaussian process modeling, Computer Methods in Applied Mechanics and Engineering 383 (2021) 113915.

[44] D. G. Giovanis, I. Papaioannou, D. Straub, V. Papadopoulos, Bayesian updating with subset simulation using artificial neural networks, Computer Methods in Applied Mechanics and Engineering 319 (2017) 124–145.

[45] C. Pepi, M. Gioffre, M. Grigoriu, Bayesian inference for parameters estimation using experimental data, Probabilistic Engineering Mechanics 60 (2020) 103025.

[46] F. Schneider, I. Papaioannou, D. Straub, C. Winter, G. Müller, Bayesian parameter updating in linear structural dynamics with frequency transformed data using rational surrogate models, Mechanical Systems and Signal Processing 166 (2022) 108407.

[47] Q. Han, P. Ni, X. Du, H. Zhou, X. Cheng, Computationally efficient Bayesian inference for probabilistic model updating with polynomial chaos and Gibbs sampling, Structural Control and Health Monitoring 29 (6) (2022) e2936.

[48] A. Cabboi, C. Gentile, A. Saisi, From continuous vibration monitoring to FEM-based damage assessment: application on a stone-masonry tower, Construction and Building Materials 156 (2017) 252–265.

[49] E. García-Macías, L. Ierimonti, I. Venanzi, F. Ubertini, An innovative methodology for online surrogate-based model updating of historic buildings using monitoring data, International Journal of Architectural Heritage (2019) 1–21.

[50] E. García-Macías, I. Venanzi, F. Ubertini, Metamodel-based pattern recognition approach for real-time identification of earthquake-induced damage in historic masonry structures, Automation in Construction 120 (2020) 103389.

[51] L. Ierimonti, N. Cavalagli, I. Venanzi, E. García-Macías, F. Ubertini, A transfer Bayesian learning methodology for structural health monitoring of monumental structures, Engineering Structures 247 (2021) 113089.

[52] R. Schobi, B. Sudret, J. Wiart, Polynomial–chaos–based Kriging, International Journal for Uncertainty Quantification 5 (2).

[53] B. Efron, T. Hastie, I. Johnstone, R. Tibshirani, Least angle regression, Annals of statistics 32 (2) (2004) 407–499.

[54] E. García-Macías, F. Ubertini, MOVA/MOSS: Two integrated software solutions for comprehensive Structural Health Monitoring of structures, Mechanical Systems and Signal Processing 143 (2020) 106830.

[55] N. Wiener, The homogeneous chaos, American Journal of Mathematics 60 (4) (1938) 897–936.

[56] C. Soize, R. Ghanem, Physical systems with random uncertainties: chaos representations with arbitrary probability measure, SIAM Journal on Scientific Computing 26 (2) (2004) 395–410.

[57] D. Xiu, G. E. Karniadakis, The Wiener–Askey polynomial chaos for stochastic differential equations, SIAM journal on scientific computing 24 (2) (2002) 619–644.

[58] G. Blatman, B. Sudret, Adaptive sparse polynomial chaos expansion based on least angle regression, Journal of computational Physics 230 (6) (2011) 2345–2367.

[59] V. Vapnik, The nature of statistical learning theory, Springer Science & Business Media, 2013.

[60] O. Chapelle, V. Vapnik, Y. Bengio, Model selection for small sample regression, Machine Learning 48 (1) (2002) 9–23.

[61] M. L. Stein, Interpolation of spatial data: some theory for kriging, Springer Science & Business Media, 2012.

[62] J. Sacks, W. J. Welch, T. J. Mitchell, H. P. Wynn, Design and analysis of computer experiments, Statistical science 4 (4) (1989) 409–423.

[63] C. Argyris, C. Papadimitriou, P. Panetsos, P. Tsopelas, Bayesian model–updating using features of modal data: Application to the Metsovo Bridge, Journal of Sensor and Actuator Networks 9 (2) (2020) 27.

[64] J. Jang, A. Smyth, Bayesian model updating of a full-scale finite element model with sensitivity-based clustering, Structural Control and Health Monitoring 24 (11) (2017) e2004.

[65] H. F. Lam, J. Yang, S. K. Au, Bayesian model updating of a coupled-slab system using field test data utilizing an enhanced Markov chain Monte Carlo simulation algorithm, Engineering Structures 102 (2015) 144–155.

[66] H. Haario, M. Laine, A. Mira, E. Saksman, DRAM: efficient adaptive MCMC, Statistics and computing 16 (4) (2006) 339–354.

[67] A. Gelman, J. B. Carlin, H. S. Stern, D. B. Dunson, A. Vehtari, D. B. Rubin, Bayesian data analysis, CRC press, 2013.

[68] T. Ishigami, T. Homma, An importance quantification technique in uncertainty analysis for computer models, in: First International Symposium on Uncertainty Modeling and Analysis, IEEE, 1990, pp. 398–403.

[69] M. Nobahari, S. M. Seyedpoor, An efficient method for structural damage localization based on the concepts of flexibility matrix and strain energy of a structure, Structural Engineering and Mechanics 46 (2) (2013) 231–244.

[70] I. Venanzi, A. Kita, N. Cavalagli, L. Ierimonti, F. Ubertini, Earthquake-induced damage localization in an historic masonry tower through long-term dynamic monitoring and FE model calibration, Bulletin of Earthquake Engineering 25 (2020) 1103–1122.

[71] E. García-Macías, F. Ubertini, Automated operational modal analysis and ambient noise deconvolution interferometry for the full structural identification of historic towers: A case study of the Sciri Tower in Perugia, Italy, Engineering Structures 215 (2020) 110615.

[72] D. T. Bartilson, J. Jang, A. W. Smyth, Sensitivity-based singular value decomposition parametrization and optimal regularization in finite element model updating, Structural Control and Health Monitoring 27 (6) (2020) e2539.

[73] R. R. Sokal, A statistical method for evaluating systematic relationships., Univ. Kansas, Sci. Bull. 38 (1958) 1409–1438.